Politecnico di Torino

Corso di Laurea Magistrale in Ingegneria Biomedica

Academic year 2024/2025

March 2025

Imaging fingertip skin deformation in response to scanned edges

Supervisors

Prof. Demarchi Danilo

Prof. Lefèvre Philippe

Prof. Delhaye Benoit

Eng. Doumont Donatien

Candidate

Fracchia Lorenzo

ABSTRACT

Touch is a complex sensory system involving a high density of mechanoreceptors in the fingertips, which provide crucial information about the environment, such as an object's geometry, texture, and mechanical properties, as well as the nature and magnitude of interactions, offering continuous feedback during grasping and dexterous manipulation. In particular, the activity of tactile afferents has been linked to local skin deformations in the finger pad. This Master's thesis project was conducted at the Institute of Neuroscience (IoNS) of the Université catholique de Louvain, where previous studies employed a robotic platform to investigate local tangential strains of the fingertip during controlled interactions with flat transparent surfaces, enabling the acquisition of images of the skin during contact. This work extended the research to non-flat stimuli, utilizing the same apparatus. First, small bump and hole geometries were economically and reproducibly manufactured on a flat transparent resin plate, replacing the flat glass surfaces. Second, the interaction of the skin with these profiles was imaged at high spatiotemporal resolution through the plate, allowing for the extraction and temporal tracking of skin features to quantify local skin deformations. The technical challenges introduced by the employment of non-flat stimuli were addressed through the image processing techniques proposed in this study, which allowed for the successful detection and identification of consistent and recurrent deformation patterns associated with the specific profiles analyzed.

Acknowledgements

Contents

List of Figures

List of Tables

1 Introduction

Tactile exploration involves sophisticated interactions between the skin and the surface of the object under inspection. Mechanoreceptors located beneath the fingertip skin are capable of detecting local stresses and deformations of the skin resulting from the contact, and generate afferent signals which provide exhaustive information about the shape, texture and mechanical properties of the surface. The nature of these interactions has been largely subject of study with the aim of understanding the skin behavior and mechanical properties during touch, and moreover their correlation with the mechanoreceptors sensing and signaling activity. Delhaye *et al.* [1] studied surface skin deformations under both normal and tangential loading of the fingertip, recording images through flat transparent plates using a custom robotic platform. They focused on the quantification of skin local slips phenomena occurring under tangential stimulation and found specific strain waves starting from the periphery of the contact area between the skin and the stimuli and moving inwards to the center of the fingertip, following the typical transition between partial and full slippage of the contact area [2]. These strains patterns were then later correlated to the activity of fast adapting (FA-I and FA-II) and slow adapting (SA-I and SA-II) afferents, by directly recording with microneurography their action potentials, after precise localization of their receptive field on the fingertip [3]. They found that FA-I activity was synchronized with local strain rates in the corresponding receptive fields and showed particular sensitivity to local skin compression and, more moderately, to stretch. They also observed higher responses of FA-I to preferred orientations of skin compressive strains. The activity of these afferents in response to local slips is thought to provide crucial and useful information for the brain to infer the friction between the finger pad and the surface of an object during its manipulation and therefore to accordingly adjust the intensity of the force applied to hold it, avoiding losing grip. The same experimental set-up was also utilized to investigate human perception of slippage while simultaneously recording images of the finger pad deformations [4] and to examine shear strains of the skin under pure torsion [5].

The purpose of this research was to extend, making use of the above-mentioned apparatus, the study of the strains tangential to the skin surface when the finger pad is in contact with non-flat stimuli, that is, stimuli with specific geometries, mimicking tactile exploration over variegated shapes.

Non-flat stimulation was already investigated in the literature. Corniani *et al.* [6] were able to image sub-surface deformations of the skin ridges when in contact with small edge and holes (1 *mm* wide and 0.3 *mm* high/deep) on a transparent plate, by means of Optical Coherence Tomography (OCT). They obtained cross-sectional scans of the skin sub-layers and quantified the strains associated with individual ridges during contact with the two shapes.

Concerning deformations of the skin tangential to its surface, Léveseque *et al.* [7] imaged skin interaction with glass transparent surfaces in the shape of small bumps and holes with Gaussian profiles, roughly 3 *mm* wide and 0.5 *mm* high/deep, in comparison with flat surfaces as well. They were able to extract features from the finger pad images, triangulate them and evaluate the strains through the frames as changes in length of the edges of the triangles. They found patterns of compressive strains when the skin was passing over the profiles rising edge, with respect to the finger direction of motion, and of tensile strains when passing over the falling edge.

The present study was intended to take advantage of the high spatial-temporal resolution of more recently developed strain analysis techniques [1] to investigate again surface skin deformation with shapes similar to those used in Lévesque *et al.* research.

This work thus aimed to find easy and reproducible ways to manufacture custom shapes with transparent materials as well as deal with the challenges of capturing images and computing strains through non-flat transparent surfaces, enabling to further expand the research with different profiles in an accessible manner. Moreover, the goal was to identify and quantify clear surface skin deformations patterns associated with the contact with two different geometries, a bump and a hole, in order to possibly correlate in future works these strains patterns to subjects' perception and discernment of shapes as well as the triggering of afferents activity. Indeed, it is reasonable to believe that the sensitivity of FA-I afferents to compression and, partially, to stretch of the skin could not only allow local slips detection during object manipulation, but also provide useful information about shapes and textures during tactile exploration.
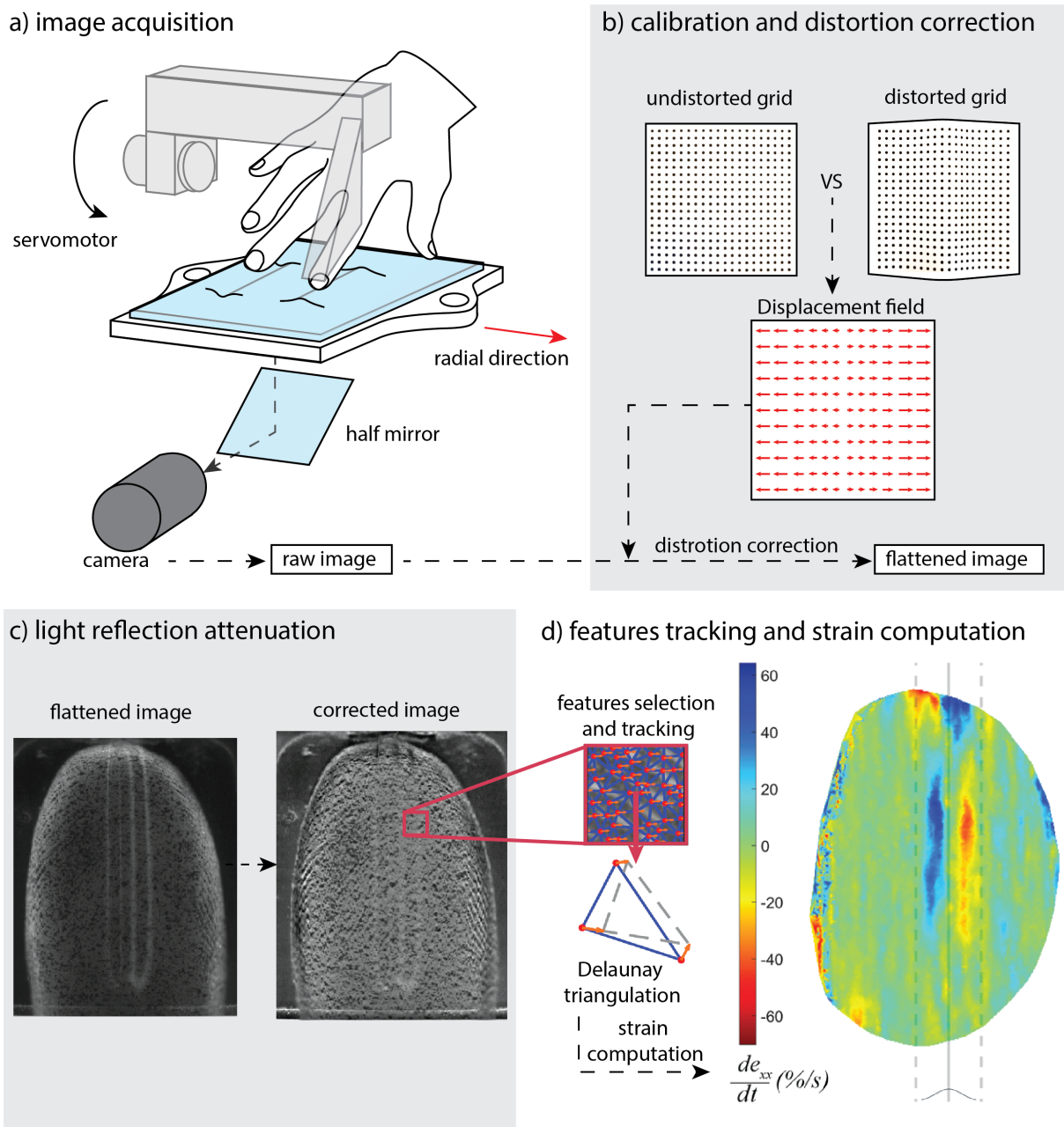
2 Materials and Methods

In this section, a comprehensive description of the experimental set-up and stimuli man-ufacturing process is provided. Next, the experimental procedure is outlined. Finally, the methods for data processing and analysis are detailed, including image processing techniques, features selection and frame-by-frame tracking, and the computation of local strain rates to quantify lateral skin deformations. Figure 1 provides a summary of the methodological framework.

2.1 Apparatus

The apparatus utilized in this study has been described thoroughly in previous publica-tions [2, 1, 4, 3, 5]. A stimulation plate was mounted horizontally on the end effector of an industrial robot (SCARA denso HS-4535G) with 4 degrees of freedom (translation along the three main axes and rotation along the vertical axis) and two force/torque transducers (ATI nano 43) were fixed to the support hosting the plate. These sensors allowed to acquire signals of the tangential and normal forces applied to the plate at a sampling frequency of 1 kHz. The participant's right index finger was secured in a custom hand support and the fingertip was pressed against the plate at a constant force, by feeding back the normal force signal to a closed-loop servo mechanism consisting of a PID controller. The images where captured through the plate itself by means of a high resolution camera (JAI GO-5000M-PMCL, 2560×2048 pixels of resolution, up to 107 frame per seconds) and a 45° half mirror. LED strips lights were mounted on top of the half mirror as well as on a u-shaped support around the finger to illuminate the scene. The imaging system was arranged in such way that a resolution of $\sim 80\ pixel/mm$ was achieved and in each trial the finger pad was fully visible, as well as two paper bands of reference markers, at the extremities of the image. Figure 2 shows the whole apparatus and a close-up of the participant's finger on the plate.

In the above-mentioned publications, the plate was made of smooth flat glass, which, for the purposes of this experiment, was substituted with a resin plate with specific stimuli manufactured on its surface, as described in details in the following Section.

a) image acquisition

servomotor

radial direction

half mirror

camera → raw image

b) calibration and distortion correction

undistorted grid   distorted grid

VS

Displacement field

distrotion correction → flattened image

c) light reflection attenuation

flattened image   corrected image

d) features tracking and strain computation

features selection and tracking

Delaunay triangulation

strain computation

$\frac{de_{xx}}{dt}\ (\%/s)$

Figure 1: *Summary of methods. a) image acquisition setup, comprising the camera, the stimuli plate on its robotic support and the servo-controlled hand support. Images of the finger pad are acquired at high spatio-temporal resolution. b) calibration phase to obtain the displacement field, which is applied to each image to flatten the stimuli 3D surface on the image plane. c) light attenuation phase, to remove the light reflection bands from the images. d) features are selected from the first image and and tracked frame by frame for each trial. After triangulation, the strain rates are derived to quantify the skin deformation.*
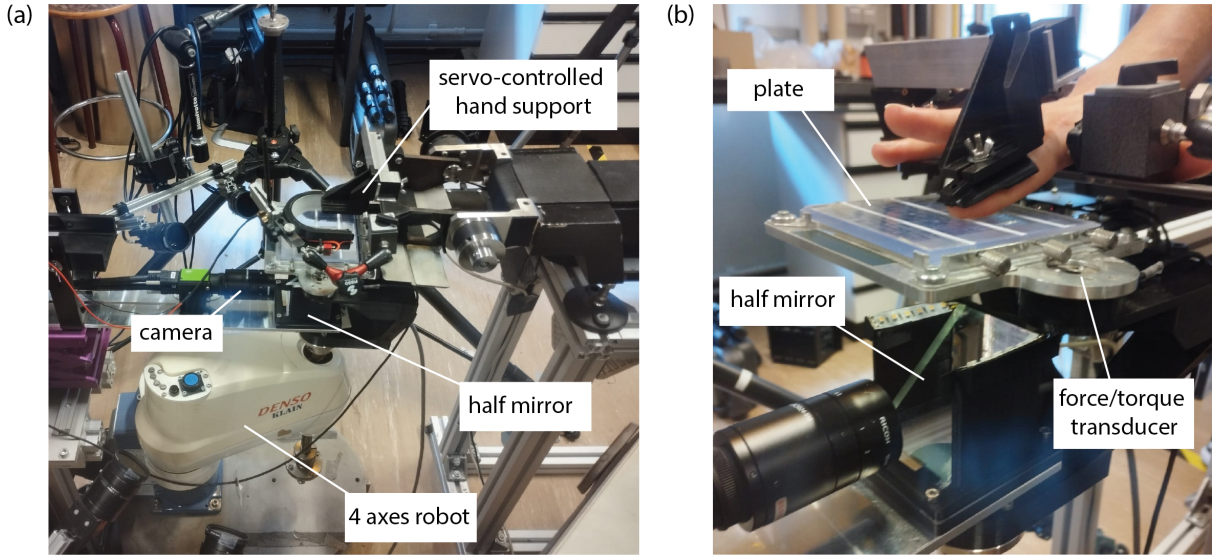
Figure 2: *Apparatus. (a) full set-up. (b) close-up, after removal of the u-shaped LED support, of the the right index finger on the plate*

2.1.1 Stimuli Plate Design

Three different stimuli were designed, in the shape of a bump, a hole and a dot. The first two were subject of this study, the latter was manufactured for possible future works. All designs were based on the same Gaussian cross-section (Figure 3.a), largely inspired to those used in Lévesque *et al.* experiment [7]:

$$y(x) = 0.5mm \cdot e^{-\frac{x^2}{(0.8mm)^2}} \tag{2.1}$$

The bump and the hole are respectively convex and concave extrusions of the cross-section on the plate surface, while the dot was obtain as a revolution of the cross-section around the vertical axis. As shown in Figure 3.b, 3-D CAD's of several prototypes consisting of plates of different sizes were iteratively designed in SOLIDWORKS environment to test the manufacturing procedure and the quality of the outcomes. The final 3D model, illustrated in Figure 3.c, is a 100 *mm* x 100 *mm* x 5 *mm* plate, to fit the support properly and be sufficiently rigid. Indeed, early 100 *mm* x 100 *mm* prototypes with smaller thickness (1 *mm*) were also manufactured, but when loaded during test trials they undesirably bent under the finger. The final plate presents a band with one 20 *mm* long hole and one bump of the same length, parallel to each other and separated by 19 *mm* , as well as a second band with two identical dots aligned with the hole and the bump. The relative position between the stimuli and their length were chosen as a

trade-off between taking advantage of the room at disposal on the plate, having designs of reasonable size compared with that of the fingertip and keeping everything compact enough so that the camera could be placed not too far from the plate and guarantee a sufficient resolution (~ 80 $pixels/mm$). Very thin and shallow lines and ticks (0.25 mm thick and 0.30 mm deep) were also engraved on the surface to facilitate the placement of the paper markers necessary for the trials.
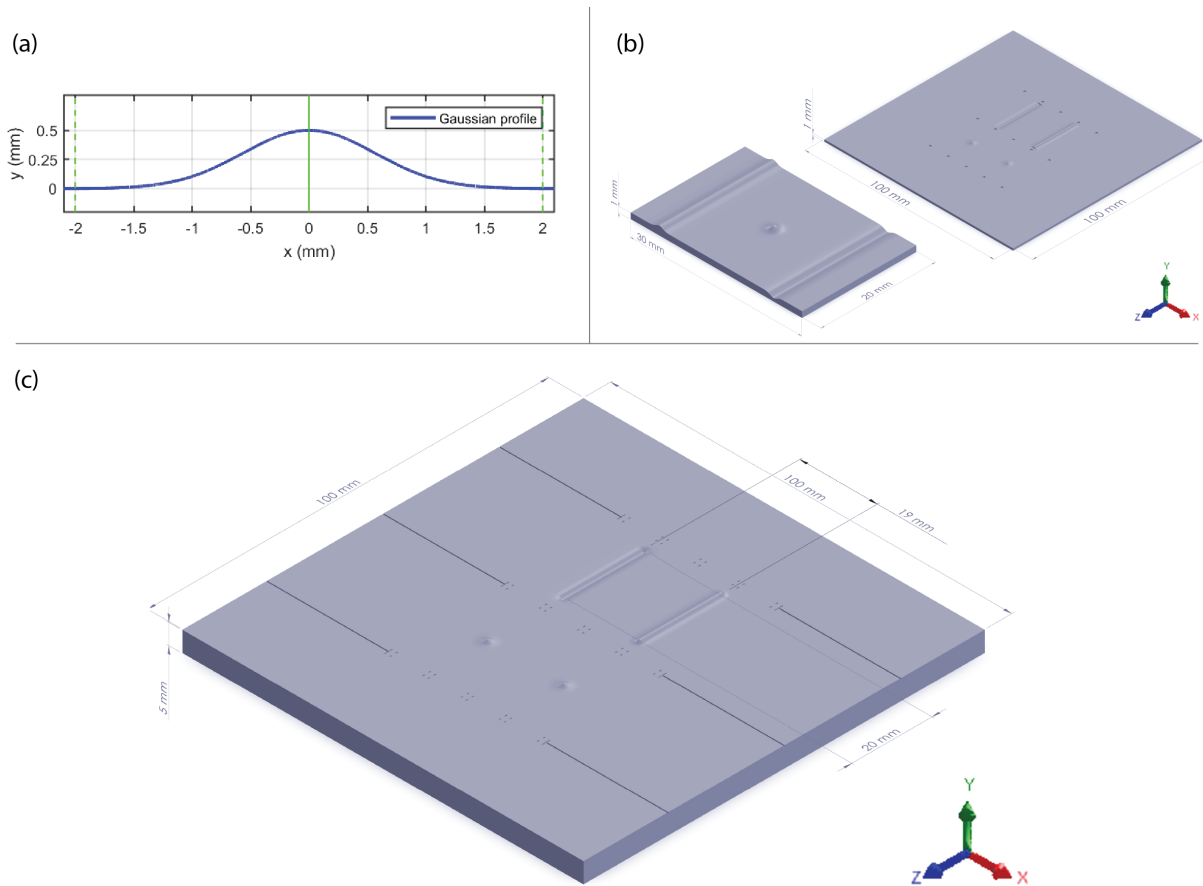
Figure 3: *Prototypes and plate design. (a) Cross-sectional Gaussian profile. The bump, the hole and the dot all share the same cross-section. (b) 3D CAD's models of some of the prototypes manufactured for testing. (c) 3D CAD model of the final plate design*
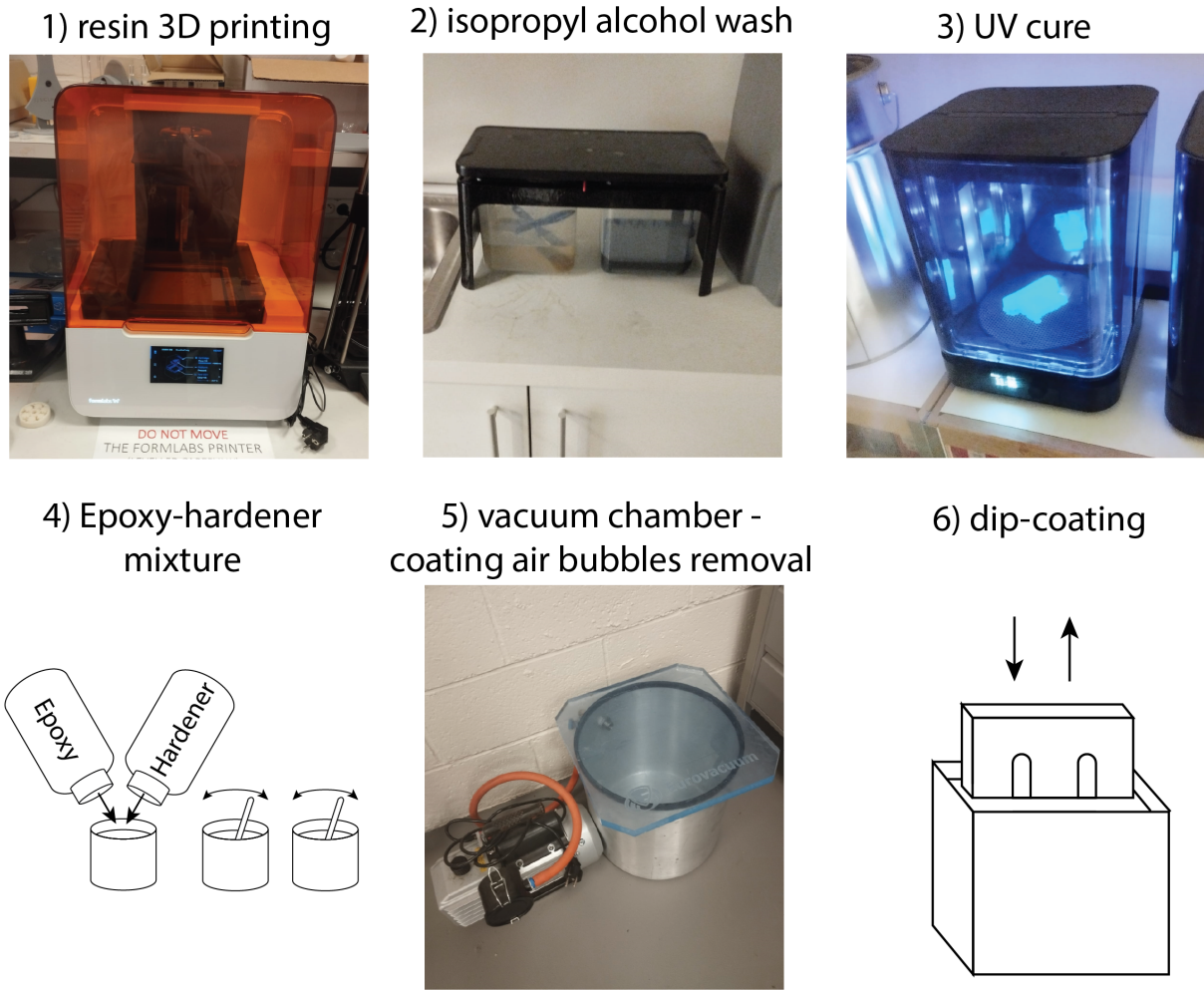
2.1.2 Plate Manufacture

The flat plates used in previous experiments were made of glass [2, 1, 4, 3, 5]. Although glass was taken into account in early phases of the manufacture process design, the cost, time and complexity of machining sophisticated shapes onto a glass surface led to the search for less expensive and more easily reproducible materials and techniques. Eventually, stereolithography with resin was chosen as the best option for its affordability and practicality. The technology allows to obtain 3D parts by means of a laser that, layer-by-layer, polymerises a liquid photo-polymer (i.e. the resin). Several tests were performed with different resins and the final product was 3D printed with Dental LT Clear resin using a Form 3B+ printer by Formlabs.

As introduced before, with small thicknesses the resin plate was too compliant and consequently bent when subject to the forces involved in the experiment, compromising the trials. The final thickness of 5 mm that provided the necessary rigidity was not problematic for the success of the experiment and simply required more material.

After the extraction from the 3D printer, the polymerization process initiated by the laser was not complete. The part therefore was later carefully cleaned to remove the liquid resin residue on its surface. The part was first sprayed on with isopropyl alcohol and then dipped in two successive baths of the same alcohol to gradually remove all the residue. Next, the cleaned part was irradiated with UV light to complete the polymerization process using the post-cure machine Form Cure.

The resulting plate was indeed made of transparent resin, but because of the layer-by-layer printing technique, the resulting surface roughness caused scattering of the light passing through and led to a translucent effect, blurring the images acquired though it and thus compromising the success of the experiments (Figure 5.a). The part was therefore coated with a transparent epoxy resin (SANAAA Clear Hard Epoxy for Casting) to restore the transparency.

The epoxy comes in liquid form and needs to be mixed with a liquid co-reactant. The reaction, referred to as curing, allows cross-link creation between the polymers constituting the epoxy which therefore hardens. To obtain a uniform and smooth coating, the plate needed to be dipped into a bath filled with a 1:1 mixture of the two reactants, while the curing process was still at an early stage and the mixture still liquid.

1) resin 3D printing   **2) isopropyl alcohol wash**   **3) UV cure**

4) Epoxy-hardener mixture   **5) vacuum chamber - coating air bubbles removal**   **6) dip-coating**

Figure 4: *Manufacturing steps. (1) The part is printed in Dental LT Clear with stereolithography using a Form 3B+ printer. (2) The part is carefully washed in isopropyl alcohol baths. (3) The part is irradiated with UV light to complete the polymerization process. (4) Epoxy and its hardener are mixed in parallel in several mixing cups. (5) The air in the epoxy-hardener mixture is removed by means of a vacuum chamber. (6) the part is dipped in and extracted from the mixture. A thin coat of epoxy is a applied on the surface.*

To minimize the quantity of materials used, a container with an aspect-ratio similar to that of the plate was utilized for the bath, which required about 500 mL of reactants to fully cover the whole plate during the dip-coating. The mixture needed to be carefully prepared to ensure the success of the process. First, the epoxy was mixed with the hardener in several different mixing cups by gently and evenly stirring the two reactants with a wooden stick, to reduce the amount of undesired air introduced inside. Nevertheless, a significant amount of air got inside the mixture and therefore the mixing cups had to be put in a vacuum chamber to remove the air bubbles. This step was particularly critical since the several depressurization cycles necessary to extract as much air as possible had

to be done in a limited amount of time, in order to prevent the mixture from becoming excessively viscous, hindering the dipping phase. In this regard, the required total amount of mixture was split in multiple cups to slow down the curing process. Indeed, the reaction is faster at higher temperatures and exothermic as well; therefore, with bigger volumes of reactants, bigger amount of heat is generated, the temperature of the mix increases and the reaction occurs faster and faster.

All the cups were prepared at the same time and were subjected to the air removal cycles in the vacuum chamber simultaneously. Next, the mixing cups were poured into the container and the plate was immediately dipped in the bath, held inside for few seconds and extracted. By doing so, a thin layer of epoxy uniformly covered the plate, filling in the irregularities at the interface of the two materials and guaranteeing a smooth outer surface, ensuring transparency of the final product. The part was maintained in a fixed position for several hours until the end of the curing process, after which the coat was completely hardened and the plate was ready to use. Figure 4 illustrates all the production steps described above.

Panels b and c of Figure 5 display respectively the effect of the epoxy coating on the surface as well as the final plate mounted on its support.
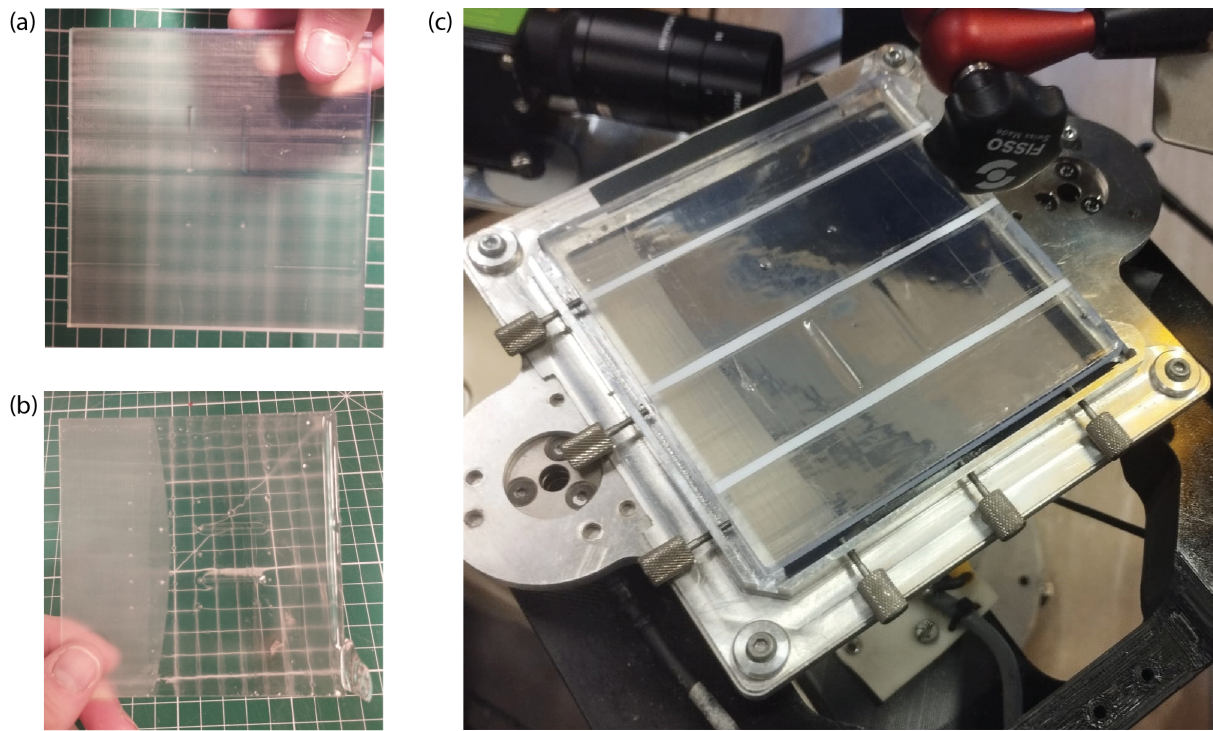
Figure 5: *Transparency recovery and final plate. (a) Plate appearance before epoxy coating. The part is translucent, blurring the image underneath it. (b) Test plate after partial dipping in epoxy. The transparency is successfully recovered. (c) Final plate, after dip-coating, mounted on its support.*

2.2 Experimental Procedure

The experiment was performed on a healthy male subject aged 24. The fingertip of the participant's right index was sprayed with black ink by means of an airbrush before the beginning of the experimental protocol (see Section 2.3.3). Two stimulation configurations were investigated: the bump to hole configuration, referred to as *BH*, which consisted in the finger pad moving from the bump to the hole, and the hole to bump configuration *HB*, consisting in a movement from the hole to the bump.

The following steps were performed for each trials. (i) Normal loading: The stimuli plate was loaded on the subject's left index pad, in correspondence of one of the two stimuli, at a fixed normal force W, which was kept constant throughout the trail thanks to the servo-controlled system as described in Section 2.1. The plate position was properly adjusted so that the stimulus profile could be completely covered by the finger pad. This step was executed over a period of time of 3 s, to ensure full loading of the fingertip onto the stimulus.

(ii) Tangential plate displacement: the stimuli plate was then moved in the radial direction R (i.e. in the direction of the thumb with respect to the fixed finger) at a constant speed, which was achieved after a transient of less than 770 ms. The plate performed a displacement of 33 mm, in such way that the finger pad could leave the first stimulus, travel over the second one and get past it completely.

(iii) Unloading: the normal force servo-controller was turned off and the plate was moved away.

A schematic of the procedure is displayed in Figure 6.

For each stimulation configuration, the procedure was executed with combinations of varying loading forces (1 N and 5 N) and constant speeds (5 mm/s and 10 mm/s), as described in Table 1. Given the camera frame rate of 50 $frame/s$, the last column of the Table reports also the number of frames for each mm of plate displacement for each condition. Each *force-speed* condition was repeated 5 times, obtaining a total amount of 30 trials (2 stimuli configurations $\times$ 5 repetitions $\times$ 3 force-speed conditions). Trials of the same stimulation configuration were executed in randomized order and the stimuli plate was mounted on the robot end effector support differently for the two configurations: for the *HB* trials, the plate was rotated of 180° with respect to the *BH* trials, to maintain the radial direction during the displacement between the two stimuli.
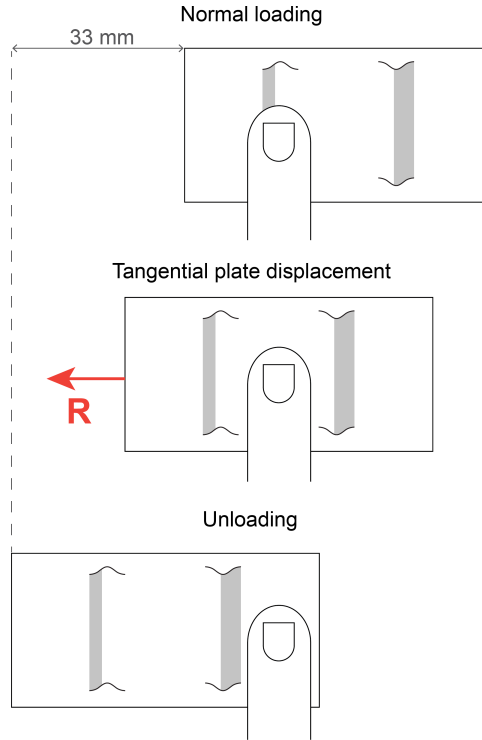
Figure 6: *Protocol steps. Normal loading of the finger pad on the first stimulus, tangential plate displacement of 33 mm in the radial direction across the second stimulus and unloading of the finger pad.*

Stimulation configuration	Trials repetitions	Normal Force W (N)	Plate speed (mm/s)	frames per traveled mm (frames/mm)
BH	5	1	5	10
	5	1	10	5
	5	5	5	10
HB	5	1	5	10
	5	1	10	5
	5	5	5	10

Table 1: Experimental procedure

After acquisition, each trial was split in two halves, the first being the Loaded condition, corresponding to the finger initially loaded on the first stimulus and experiencing the 'stick-to-slip' transition [2, 1] while the first stimulus moves away, and the second

being the Sliding condition, corresponding to the second stimulus moving across the full width of the finger pad in full slip regime. The analysis was therefore performed on the resulting set of 60 trials, summarized in Table 2.

Finger Condition	Stimulus	Trials repetitions	Normal Force W (N)	Plate speed (mm/s)	frames per traveled mm (frames/mm)
Loaded	B	5	1	5	10
		5	1	10	5
		5	5	5	10
	H	5	1	5	10
		5	1	10	5
		5	5	5	10
Sliding	B	5	1	5	10
		5	1	10	5
		5	5	5	10
	H	5	1	5	10
		5	1	10	5
		5	5	5	10

Table 2: Final set of Trials

2.3 Data Analysis

2.3.1 Distortion Correction

Stimuli profiles and their manufacture introduced distortions that had to be taken into account to properly track features and compute the strains.

Indeed, the relative distances and areas between points belonging to a stimulus surface in 3D space appear distorted in the images captured by the camera because of their projection (geometric distortion) on the image plane and the effects of light refraction at the interface between the plate material and the coating material (light distortion). A calibration grid, consisting of small black dots spaced by 0.25 mm and printed on paper, was used to correct the overall distortion. Such calibration grids have been widely used to correct optical deformations in a variety of applications, as well as in the specific context of skin deformation imaging [7, 8].

Specifically, the two stimuli were designed as *developable surfaces*, that is, surfaces that can be mapped isometrically onto a plane, therefore allowing to roll a planar grid on top of them avoiding any warping [9].

The grid was applied to the stimuli, after being dipped in water to ensure that it adhered to the surface of the plate, and pictures of the distorted grids were taken. Images of the same grids on a flat glass surface were also captured as corresponding undistorted 'ground truths'. The distorted and undistorted grids were converted to binary images to identify the dots, and the center of each dot was derived from the mean of its x and y pixel coordinates. The displacement fields was obtained computing the distances between corresponding dots in the distorted grids and undistorted grids and were then used to correct each frame of the trials. Figure 7 shows the distorted and undistorted grids for both designs (panels a and c), as well as the displacement fields obtained after calibration (panels b and d), with the corresponding components along the x-axis (u-displacement, averaged along the y-axis) and y-axis (v-displacement, averaged along the x-axis).

Predictably, the average v-components is close to zero for both profiles. The curves of the u-displacement were initially expected to be the same for both designs, given the symmetry of their geometry. Instead, their trends appear to be different. Indeed, the thin layer of epoxy applied on top of the plate resin, assuming that the two materials have different refraction indices, causes light refraction at the interface of the two media,
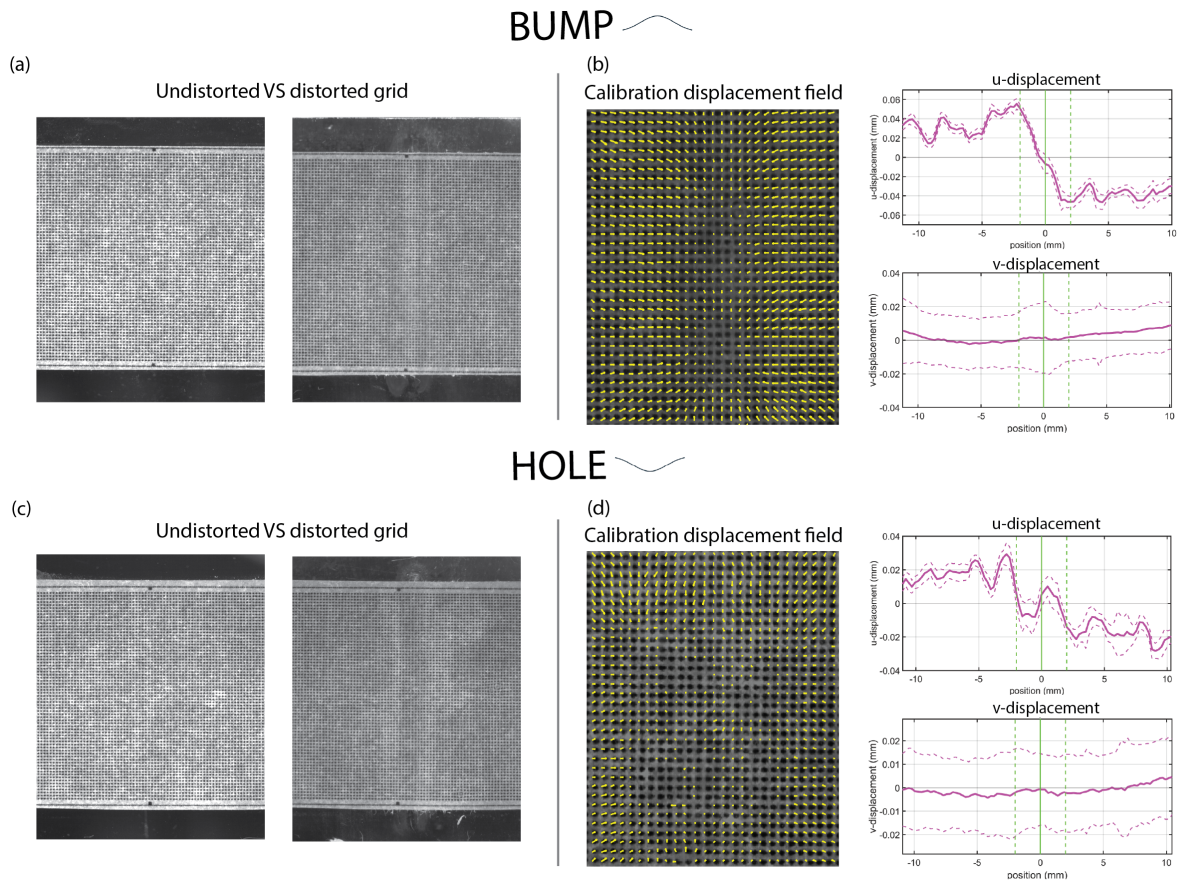
Figure 7: *Calibration grids and displacement fields. (a) and (c), the undistorted and distorted grids side by side for bump and hole, respectively. (b) and (d), the calibration displacement fields obtained from the grids, as well as their average u and v component, for bump and hole, respectively, with the corresponding standard deviations in dotted lines. In all plots, the green solid line and the two green dotted lines represent, respectively, the center and the two extremities of the stimuli.*

leading to different overall displacements for the two geometries.

The actual relative distances between the features over the two stimuli surfaces are deformed by their corresponding overall displacement field, causing artifacts in the computation of the strains and thus misinterpretation of the actual deformations of the skin. Therefore, these deformations need to be corrected before the feature tracking and strain computation phases.

To achieve this, two white paper strips with black markers were taped on the plate at the extremities of the stimuli. A semi-automatic algorithm was developed to recognize and track the markers frame by frame in a similar fashion as the dots of the calibration grids. From the markers positions at a given frame, the coordinates of the stimulus center were precisely located (Figure 8.a). Next, in each frame in which a stimulus appeared, the

corresponding displacement field obtained from calibration (changed in sign) was applied to the image, after matching the center of the field with the center of the stimulus in that frame. By doing so, the surface of the stimulus was 'flattened' on the plane of the plate, avoiding the artifacts described above. Figure 8.b highlights the transformation of a frame before and after the correction. Even though the displacements applied to each position in the frame are small (just few pixels), the effect of the displacement correction on the computation of the axial strain rate along x ($\frac{d}{dt}e_{xx}$) is still significant, especially for the hole design. Figure 8.c compares the strain rate evolution computed on the same frames of a hole trial before and after the frame by frame displacement correction. A clear pattern of artifactual $compression - stretch - compression$ can be observed in the strain rate computed on the raw images, which is strongly attenuated after the correction.

In principle, the displacement fields could also be obtained mathematically, provided that the geometry of the profile, the thickness of the epoxy layer and the refractive indeces of the epoxy and the resin are known. Specifically, the geometric and light displacements can be modeled along a given horizontal line as a function of x, and reproduced along the vertical axis (y coordinate) for the whole length of the stimuli, given that they were designed as developable surfaces. This alternative approach is discussed in Appendix A.1. Moreover, it was possible to utilize the calibration grid discussed above because of the developable property of the surfaces adopted in this experiment, allowing to easily and properly lay on top of them a planar grid without any deformation of the paper, which would compromise the correct reconstruction of the distortions. Instead, the employment of a calibration grid is generally not possible with other kinds of stimuli with non-developable surfaces which might be of interest in the context of tactile exploration. A possible solution for a generic 3D profile is proposed in Appendix A.2, provided that its geometry and the thickness of the epoxy layer are known and the two materials have similar refractive indeces.
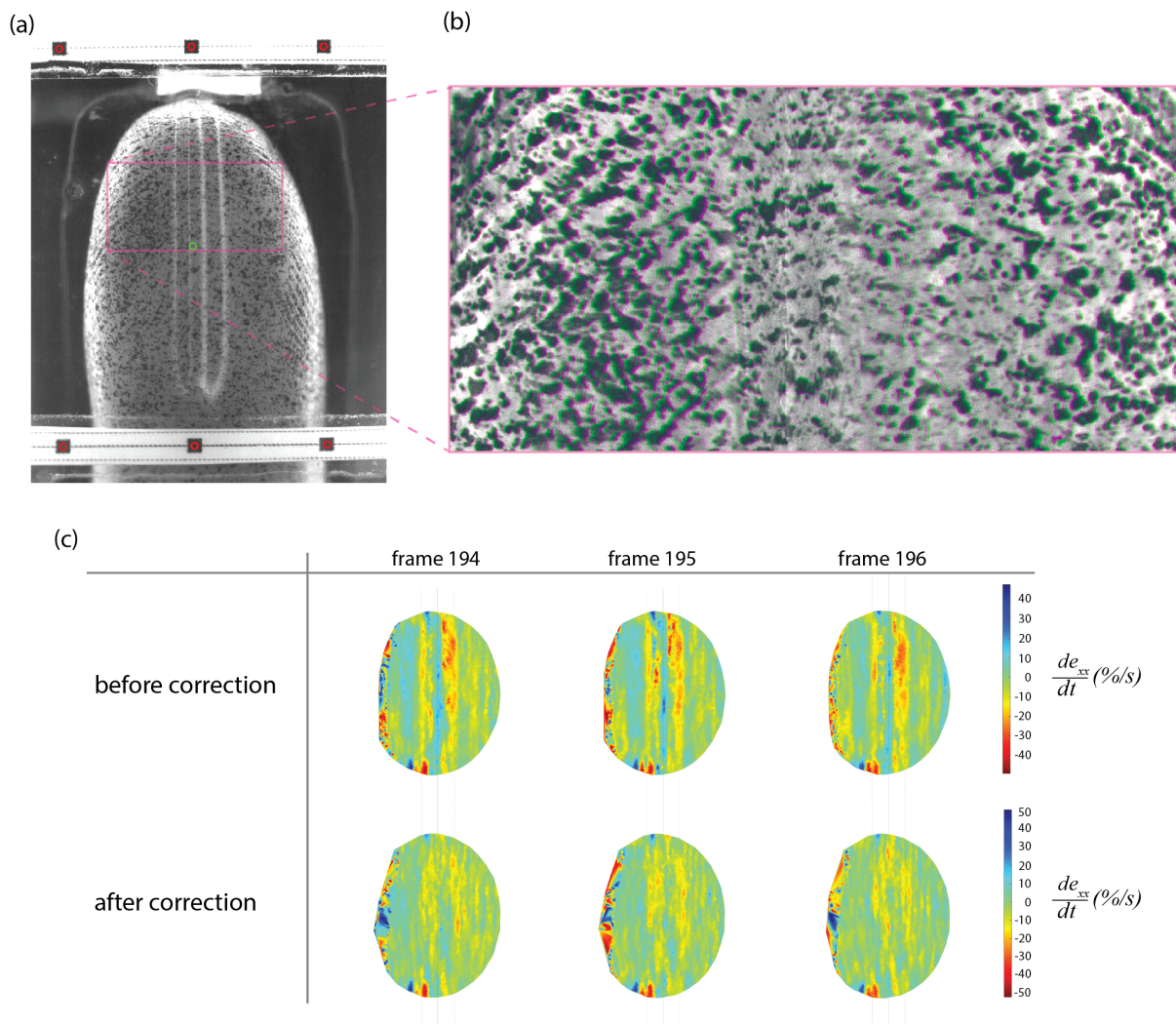
Figure 8: *Frame by frame distortion correction. (a) Bump trial frame. In red circles, the reference markers localized by the semi-automatic algorithm. The green circle represent the center of the stimulus, computed from the reference markers positions. (b) Close-up on a region of the finger pad. The raw and flattened images are superimposed and their pixel-wise difference is indicated by green and magenta pixels. The two images where also corrected from light reflections as in section 2.3.2 for visualization purposes. (c) Strain rates before and after distortion correction. The x component of the strain rates was computed for the same three consecutive frames of a hole trial, before correction (upper line) and after correction (lover line).*

2.3.2 Light Reflection Attenuation

The LED illumination of the set-up necessary to acquire the images caused light reflections in correspondence of the stimuli profiles, which hindered proper features tracking in the areas affected by the reflections. Therefore, the reflections necessitated attenuation to avoid the resulting incorrect strain computation in those areas.

During early tests with no attenuation, the intensity of the reflections was too high and resulted in bands of completely saturated pixels and the consequent loss of information of the features passing through them. Therefore, stripes of paper were placed in front of the LEDs to diffuse the light and obtain an initial attenuation of the intensity of the reflections. By doing so, the pixels in the reflection bands were not saturated anymore. Nevertheless, features were still easily wrongly tracked because of the abrupt change in pixel intensity when crossing the bands. Thus, every frame was processed as explained below, in order to reduce the difference in contrast between the areas of the image involving the reflection bands and those involving the rest of the fingertip.

All images were stored as 8-bit matrices with values ranging from 0 to 255, but for the sake of simplicity, they're described as ranging from 0 to 1. Every image I, after having already undergone distortion correction as described in section 2.3.1, was multiplied by a weight map W' to obtained the corrected image I_c. The weight map was computed as follows: each frame was first convoluted with a vertical nx1 kernel to filter out the speckles pattern from the image along the main direction of the reflection bands, with n chosen as a compromise between achieving effective pattern filtration and accurately approximating the profile of the light reflection bands. The resulting filtered image I_f was then inverted to obtain a preliminary map W. Subsequently, to allow possible further tuning of the weights, the elements of W were first raised to the power of $m > 0$ and then the overall map contrast was enhanced remapping the pixel intensity histogram inside a selected input range to the output range of $[0, 1]$, by means of the MATLAB function *imadjust*, resulting in the map W'. Its darker areas, corresponding to lower weights, map the profile of the reflection bands and thus lower down the intensity of the pixels in those locations, when multiplied by the image. A diagram of the processing is proposed Figure 9. After preliminary tests the parameters were set as follows: kernel size equal to 100x1, $m = 3$ and the input range equal to $[0.05, 0.15]$.
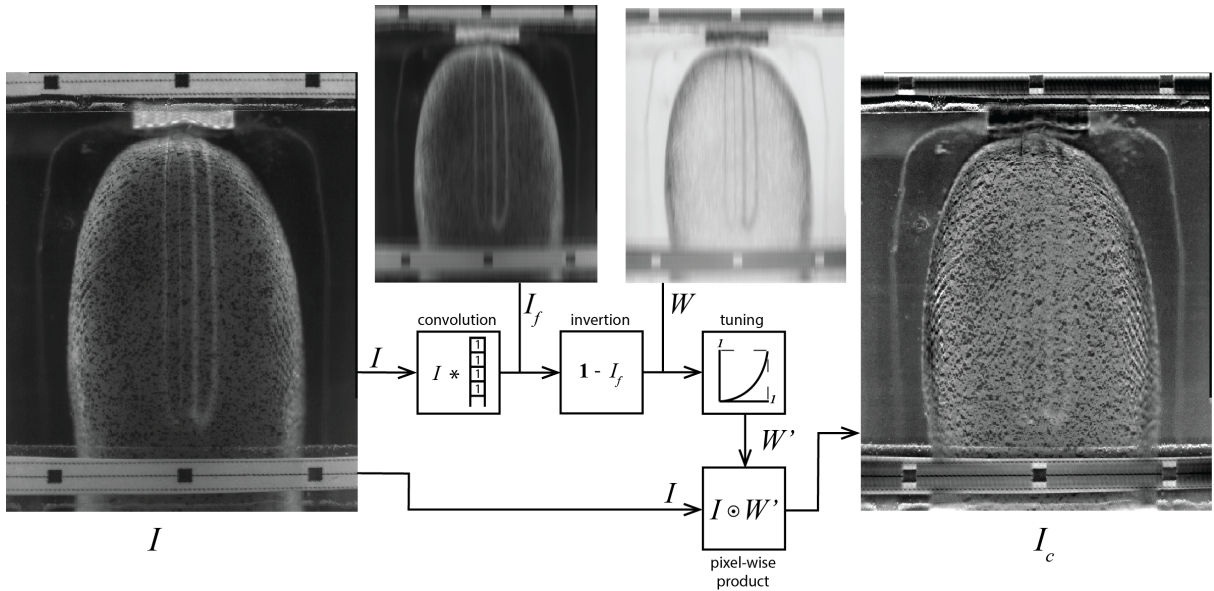
Figure 9: *Light reflection attenuation process. A schematic of the image correction process to attenuate the light reflections in correspondence of the stimuli profiles.*

The resulting corrected image therefore presents a more homogeneous contrast across the fingertip, resulting in more successful feature tracking and thus avoiding erroneous strain computations. Figure 10 compares the axial strain rate $\frac{d}{dt}e_{xx}$ computed on the same frames with and without processing the light reflections, for both the bump and the hole designs (a and b panels, respectively). The reflections caused significant artifacts in the strain rate computed from the uncorrected images, which were successfully eliminated after processing the images, allowing correct analysis of the strain rates. Specifically, in the examples shown in Figure 10, the strain rates before image correction were very noisy and difficult to interpret for the bump design, while after correction the resulting strain rates pattern is clearer and consistent among the trials. On the other hand, for the hole design, before image correction the strain rates manifest a pattern of contraction on the falling edge of the Gaussian profile and stretch on the rising edge, which disappears after processing the frames. Frame by frame light reflections correction is therefore necessary to correctly identify strain rate patterns otherwise hidden by noisy computations as well as avoid misinterpretation due to undesired strain artifacts.

24
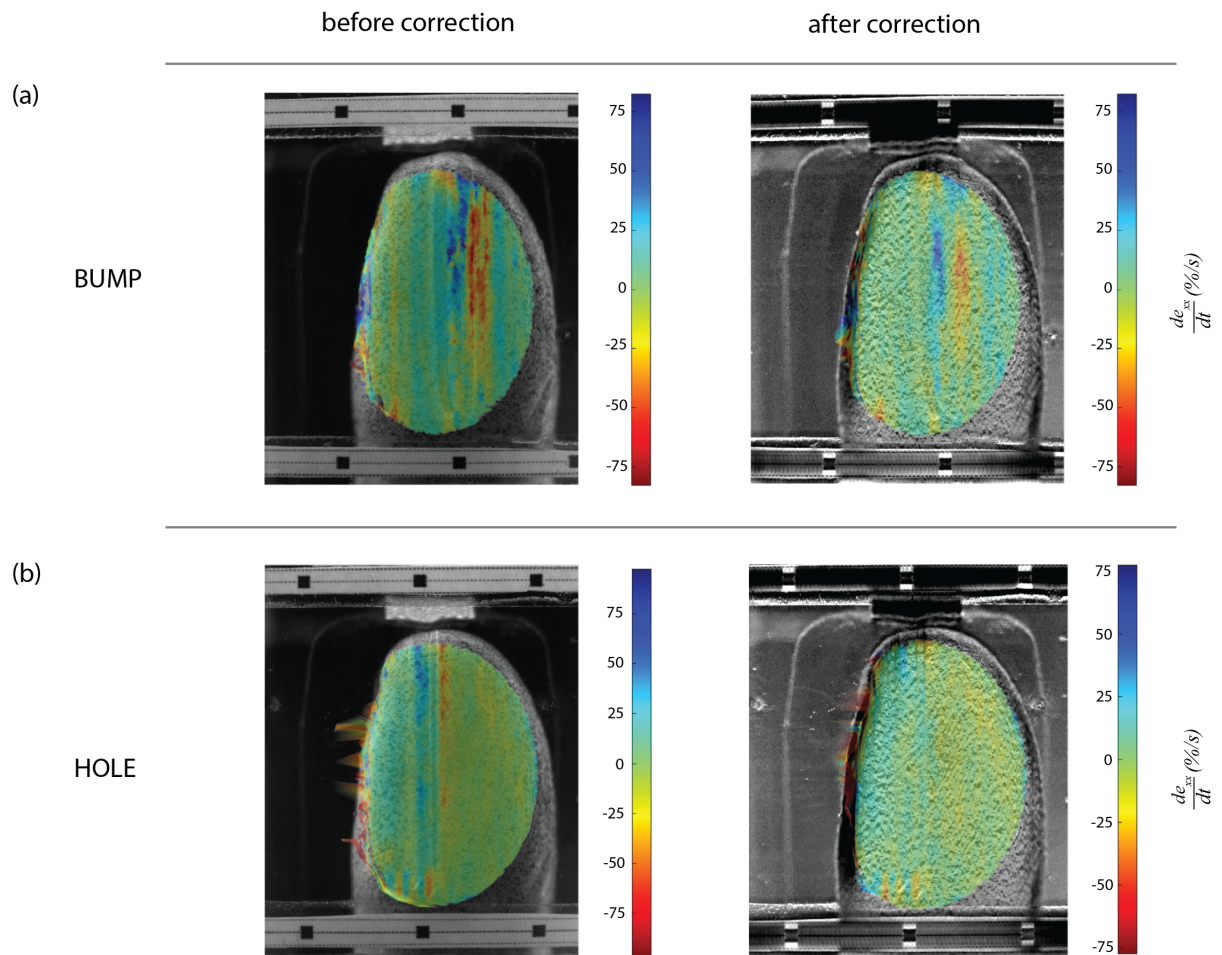
Figure 10: *Strain rates before and after light reflection attenuation. (a) Strain rates along x-axis of a bump trial frame computed before and after light reflection correction of the image. (b) Same as (a), but for a hole trial frame.*

2.3.3   Strains Computation and Analysis

Local strain rates of the finger pad were computed from the frames of each trials similarly to the previous studies of Delhaye *et al.* [1, 3], adjusting the procedure to the different nature of the images of this experiment. Indeed, in their work the strain computations relied on sampling and tracking of features based on high contrast images of the finger-pad ridges inside the contact area by means of co-axial illumination with respect to the orientation of the camera [10]. With such arrangement, light rays were reflected back in correspondence of the finger pad valleys, where no contact with the plate surface occurs, while they were mostly scattered at the interface between the plate and the ridges, therefore appearing much darker. The unique arrangement of the ridges was then utilized to sample and track features frame by frame. Additionally, the gross contact area could be estimated for each image with grey-scale morphological operations of closing and then opening. This technique was tested as well with the resin plate we manufactured, bud didn't produce satisfactory results (Figure 11). The contrast achieved between ridges and valleys was often insufficient and not consistent across the fingerprint in contact with the plate. Moreover, the manufacturing procedure caused imperfections on the plate, mostly air bubbles trapped in the epoxy coating during the curing process, that resulted in quite noisy images, compromising the extraction and tracking of features. Most importantly, the co-axial illumination ensured light reflection back in the direction of the camera only when hitting surfaces orthogonal to the rays themselves, meaning that light striking the Gaussian profiles was mostly reflected in other directions, darkening large portions of the area in correspondence of the stimuli and thus completely shadowing the ridges in the regions of highest interest for the purposes of the experiment. For these reasons, a different approach was adopted, illuminating the scene from different angles with the LED stripes. By doing so, high-contrast images of the ridges could not be captured and the finger pad itself didn't provide enough diversity in its appearance to sample reliable features for the tracking phase. Consequently, a specific speckles pattern was applied on the fingertip by spraying black ink with an airbrush.

The strains computation phases are described as follows. First, since the contact area couldn't be precisely estimated unlike in the above-mentioned works, for each trial an elliptical region of interest was selected, covering the area of the finger pad across all its frames. Next, feature points were sampled over the ROI from the first frame of the trial,

26
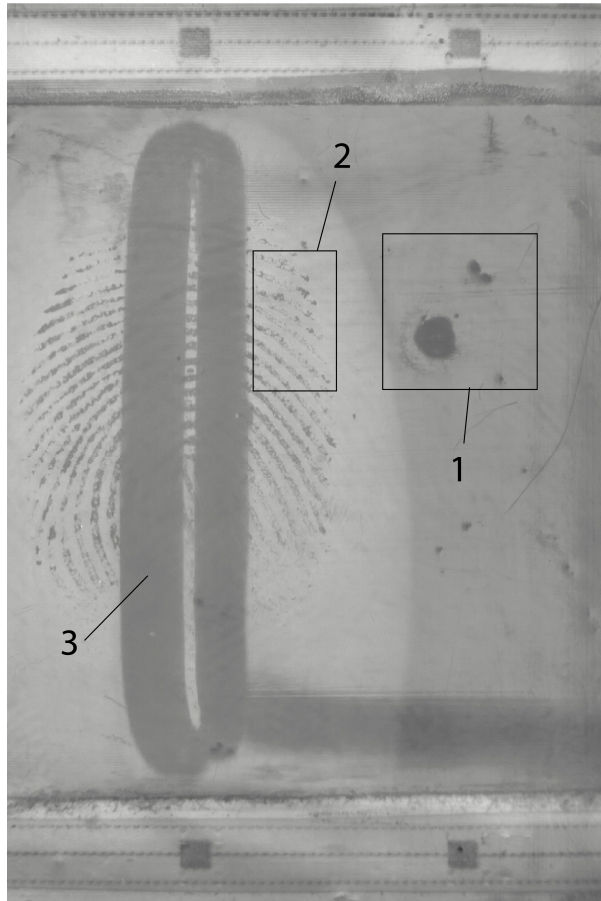
Figure 11: *Test image with co-axial illumination. (1) Air bubbles artifacts. (2) Fingerprint region in contact with the plate with unclear ridge-valley distinction. (3) Shadowing of the fingerprint in correspondance of the stimulus.*

using Shi & Tomasi's algorithm for optimal features selection [11], spaced at least by 10 pixels. Subsequently, the features were tracked frame by frame to obtain the corresponding displacement field between successive frames, employing an optical flow algorithm based on the Lucas & Kanade's method with pyramidal refinement [10, 12], implemented in the computer vision open-source library OpenCV [13], utilizing 151 x 151 pixels patches around the feature points. Features were removed if they crossed the border of the ROI or if they exhibited poor similarity between consecutive frames, achieving a number of features in the range of 5000/6000, depending on the trial. Light reflections in the stimuli area caused a change in the pixels intensity of a part (or the totality) of a feature patch passing through the reflection bands and, therefore, an abrupt loss of similarity from the previous frame, resulting in the rejection of a large amount of features. Moreover, even for the un-removed features, the optimal flow algorithm was not guaranteed to find the correct displacement of a feature across the stimuli, due to its drastic change in appear-

ance. For these reasons the images had to be corrected from the reflections as described in 2.3.2.

A triangular mesh was then constructed from the feature points in the first frame, using Delaunay triangulation, and applied to all the frame. The displacement field gradients (Equation 2.2) between each couple of consecutive frame were then computed for each triangle.

$$G_u = \left(\frac{\partial u}{\partial x}, \frac{\partial u}{\partial y}\right), \quad G_v = \left(\frac{\partial v}{\partial x}, \frac{\partial v}{\partial y}\right) \tag{2.2}$$

where u and v are the displacements along the x and y axes, respectively. Figure 12 shows a schematic of the Delaunay triangulation applied to each frame and the associated displacement fields.
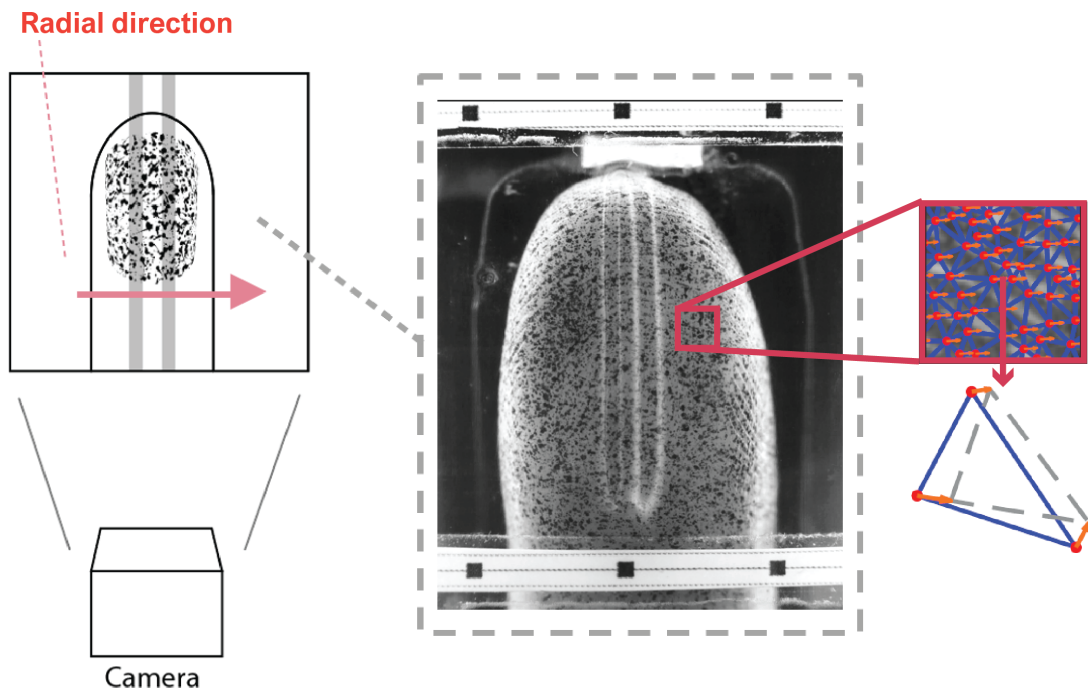
Figure 12: *Feature selection and Delaunay triangulation. The camera captures images of the finger pad. Features are selected from the speckles pattern and triangulated (Delaunay traingles shown in blue lines). Lucas & Kanade's optical flow algorithm is performed to obtain the displacement fields between consecutive frames (red arrows) associated to each triangle.*

The gradients were thereafter utilized to derive the Green-Lagrange axial strains along

the x direction e_{xx} of each triangle.

$$e_{xx} = \frac{\partial u}{\partial x} + 0.5 \left[\left(\frac{\partial u}{\partial x} \right)^2 + \left(\frac{\partial v}{\partial x} \right)^2 \right] \qquad (2.3)$$

Since the strains were computed between subsequent frames they're referred to as *strain rates* and indicated as $\frac{d}{dt}e_{xx}$. A heat map of the strain rates for each frame was therefore generated, in which colors towards the blue correspond to tensile strains and colors towards the red correspond to compressive strains.

For each trial, the strain rates heat maps of every frame were inspected to spot possible strains patterns associated with the interaction with the stimuli. Strains patterns at the periphery of the ellipse were discarded due to the high probability of loss of contact with the plate and consequent optical distortions, causing strain artifacts. When a pattern was recognized, a rectangular region of interest (ROI) was selected around it in such way that the x coordinate of the center of the ROI was aligned with the center of the stimulus along the x-axis at that specific frame. The width of the ROI (e.g. its length along the x-axis) was then divided in equally spaced sub-intervals and the strain rates inside the ROI were averaged along the y-axis for each sub-interval, obtaining an estimation of the average trend of the pattern of a given frame. Given the discrete amount of Delaunay triangles and their corresponding $\frac{d}{dt}e_{xx}$, the amplitude of the trend was sensitive to the spacing of the sub-intervals for small spacing values and generally stabilized for spacing values greater than or equal to 15 pixels ($\simeq 0.19$ mm), which was selected as the length of the sub-interval for all the trials, to maximize the resolution of the trends. Figure 13 shows a pipeline of the Strain Computation and Analysis described above.
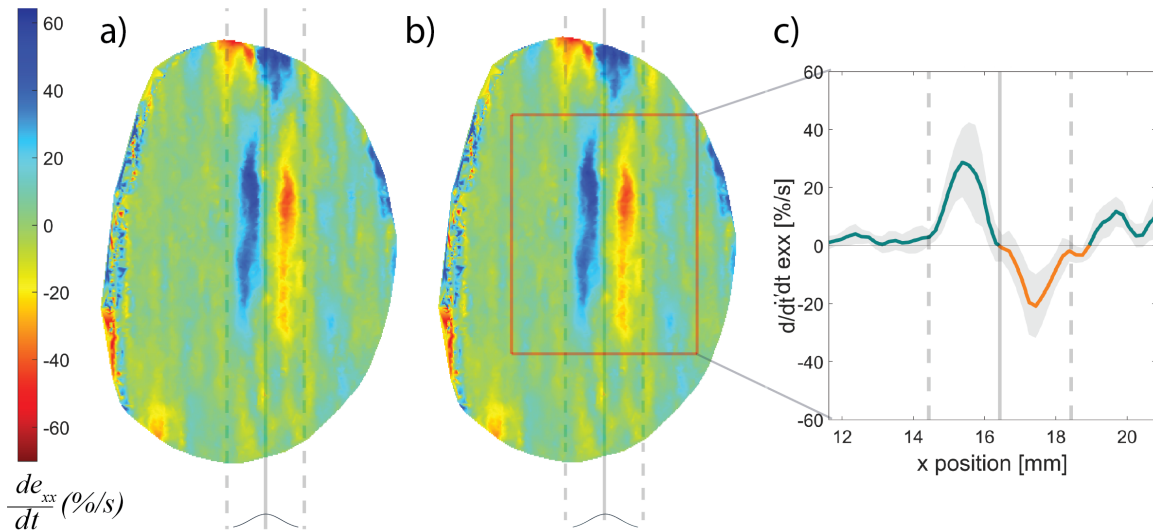
Figure 13: *Strains Computation and Analysis pipeline. a) $\frac{d}{dt}e_{xx}$ strain rates heat map of a bump trial frame. Colors towards the blue correspond to tensile strains and colors towards the red correspond to compressive strains. b) ROI selection around the strain rates pattern. c) Average $\frac{d}{dt}e_{xx}$ trend. The blue line corresponds to tension, the orange line to compression. The shaded gray area corresponds to the standard deviation computed along the y-axis at each sub-interval. For all panels, the gray solid vertical line corresponds to the center of the stimulus and the gray dotted vertical lines to its extremities.*

2.3.3.1 Stuck Area The x-coordinate of the stimulus center and of the features were low-pass filtered in the time domain (2nd order Butterworth filter with cut-off frequency of 2.5 Hz) and a relative displacement field was computed as the difference between the filtered features u-displacement field and the filtered center u-displacement field. With reference to previous studies [2], for each frame the stuck area was obtained from the features associated with a relative displacement between consecutive frames lower that 50 μm, that is, those that moved approximately rigidly with respect to the plate, and therefore considered 'stuck'. To account for unreliable relative displacement values at the periphery due to the loss of contact between the skin and the plate, the region including all features was scaled to roughly 64% of its original area and all external features were not considered. The stuck area was then computed as the convex hull enclosing the selected features.

30

3   Results

The frame by frame strain rates evolution of each trail was inspected as described in Section 2.1.2 to investigate patterns associated with the finger pad interaction with the two stimuli. Table 3 summarizes the pattern detection across all trials conditions. Considering the Sliding trials, no clear pattern was observed with 1N of Normal Force (W), regardless of the plate speed and the type of stimulus. On the other hand, distinct strain rates patterns were detected with W equal to 5N for both the bump and the hole, showing tendency of compression in correspondence of the falling edge of the stimuli (with respect to their direction of motion) and of stretch in correspondence of the rising edge, as discussed in details in Section 3.2, in accordance with previous findings [7]. Considering the Loaded trials, during the 'stick-to-slip' transition phase [2, 1] no patterns were observed either with 1N or 5N of Normal Force. After reaching full slip, in 5N trials stimuli had already extended to the periphery of the elliptical region and therefore strains patterns were discarded, while in 1N trials patterns were occasionally found with both 5 mm/s (4 trials out of 5) and 10 mm/s (4 trials out of 5) of plate speed, but solely with the bump profile, resulting in an unexpected asymmetry between the two stimuli profiles. Most importantly, the patterns showed an opposite trend (marked with a * in Table 3) of compression and stretch than what expected for the bump and what found in the Sliding conditions. For these reasons the patterns were suspected to be artifacts due to local loss of contact in correspondence of the stimuli, and therefore discarded. The cause of these artifacts is further investigated in the following Section.

Finger Condition	Stimulus	Normal Force W (N)	Plate speed (mm/s)	number of trials showing distinct patterns
Loaded	B	1	5	4* of 5
		1	10	4* of 5
		5	5	0 of 5
	H	1	5	0 of 5
		1	10	0 of 5
		5	5	0 of 5
Sliding	B	1	5	0 of 5
		1	10	0 of 5
		5	5	5 of 5
	H	1	5	0 of 5
		1	10	0 of 5
		5	5	5 of 5

Table 3: Detected patterns

3.1 Loaded condition

Loaded condition trials were characterized by the 'stick-to-slip' transition described in previous works [2], during which the skin slippage starts from the periphery of the contact area and moves inwards, progressively reducing the 'stuck' area (that is, the portion of the finger pad that moves rigidly with the plate), until full slip state is reached. This phenomenon involves the propagation, from the periphery toward the center, of typical strain waves of compression ahead of the stuck area and of stretch behind it [1]. Figure 14 shows the stick-to-slip x-axis strain rates evolution for a 1N trial (a) and 5N trial (b) with the bump stimulus. Similar results were obtained for the other Loaded condition trials. The red solid line superimposed to the strains in each frame delimits the corresponding stuck area. The transition occurred faster in trials with 1N of Normal Force than in those with 5N and no clear perturbation due to the presence of the stimuli to the stick to slip evolution was observed in all trials independently of the Normal Forces, plate speeds and type of stimulus.
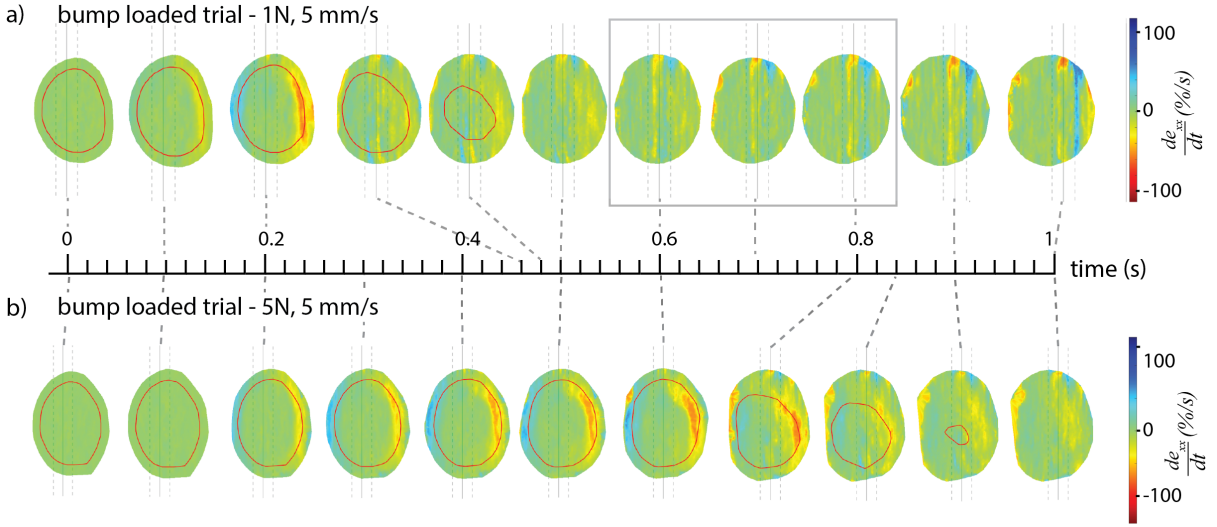

Figure 14: *Stick to slip transition. X-axis strain rate evolution in bump trials with 5 mm/s of plate speed with Normal Forces of 1N (a) and 5N (b). The stuck area is shown in red solid line, while the gray solid vertical lines correspond to the center of the stimulus and the gray dotted vertical lines to its extremities. The gray box indicates the frame span in which anomalous opposite trends where detected.*

After reaching full slip, $\frac{d}{dt}e_{xx}$ patterns in 5N trials were rejected since the stimuli were already situated at the periphery of the elliptical ROI, where the skin had likely lost its contact with the plate, while occasional patterns were observed in some trials with 1N of Normal Force for both plate speeds (5 and 10 mm/s). For the 1N trial in Figure 14.a, a

gray box highlights the span of frames in which patterns were detected after reaching full slip. These patterns inexplicably appeared only for the bump profile and, as introduced in Section 3, they seem to be in contrast with Sliding condition results (Section 3.2), in which full slip is established as well and where no patterns are observed in any of the 1N trials. Furthermore, the observed patterns in the 1N Loaded condition bump trials all showed similar trends (Figure 15.a) which are inconsistent with what expected from previous works [7] and found in Sliding condition trials. Indeed, given that the bump was moving from left to right, it was expected to generate compressive strains along the x-axis on its falling edge (its right side) , and tensile strains on its rising edge (its left side). Instead, the patterns exhibited roughly the opposite trend. For these reasons, they were concluded to be artifactual. Their trend can be explained assuming loss of contact between the skin and the bump in correspondence of its sides, thus implying that 1N of Normal Force is too light to ensure contact. Partial loss of contact with Gaussian-shaped stimuli was also observed previously [7]. The consequent gap between the skin and the stimulus, given the geometry of the bump and the difference between the refractive indices of the air and the plate resin, results in an optical distortion in correspondence of the bump sides, which travels from left to right following the stimulus movement and generates the artifactual $\frac{d}{dt}e_{xx}$ strain rates observed in the trials. To demonstrate this, a simulation of the effect on the x-axis strains computation due to a moving displacement field representing the optical distortion above mentioned was performed. For simplicity, the simulation was conducted in 1 dimension (i.e. the x axis). The displacement field was applied on equally spaced dots, therefore assuming the dots to slip over the stimulus at every instant without compressing or stretching, similarly to what happens in trials where no strain patterns are observed, and it was modeled as follows:

$$\text{light distortion}(x) = 0.4 \cdot e^{-\frac{x^2}{(0.8mm)^2}} \cdot x \qquad (3.1)$$

At each time step (corresponding to a frame), the center of the displacement field was shifted accordingly to the trials stimulus movement (0.1 mm/frame, from left to right).
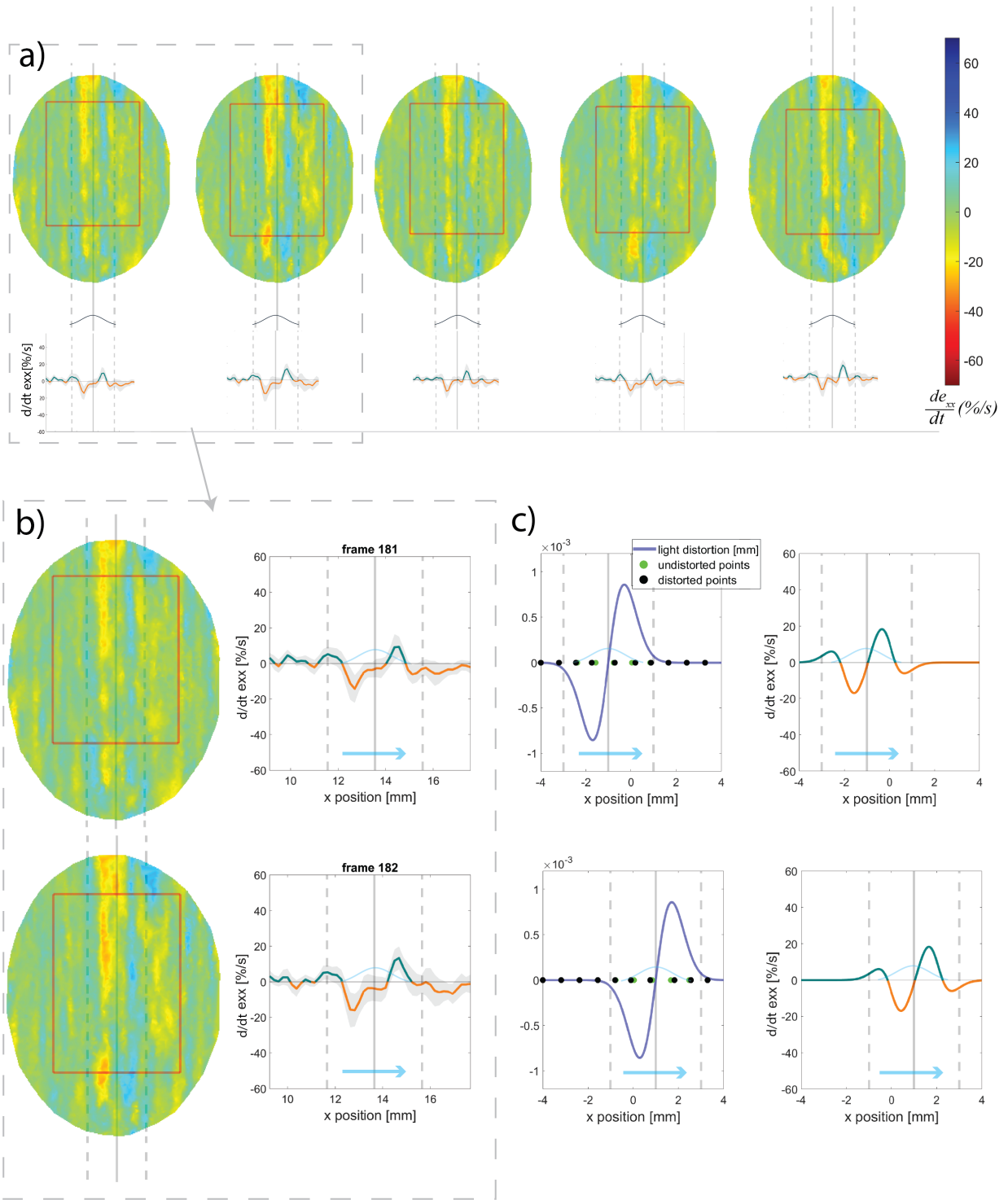
Figure 15: *Loss of contact artifacts. a) Heat maps of 5 consecutive frames of a 1N , 5 mm/s, Loaded bump trial. The corresponding average patterns are displayed underneath each heat map. b) On the left, heat maps of two frames of the same trial. On the right, the corresponding average patterns in solid lines (blue corresponding to tension and orange to compression). The shaded gray area corresponds to the standard deviation. c) On the left, the simulated light distortion displacement fields in solid light violet line at two different time steps. The undistorted dots are represented in green, while the position of the dots after distortion (in black) is exaggerated for visualization purposes. On the right, the corresponding simulated x-axis strain rates are displayed. For all panels, the gray solid vertical line corresponds to the center of the stimulus and the gray dotted vertical lines to its extremities, the bump profiles are reported in light blue solid lines without a scale solely to indicate their position and their direction of movement is indicated with light blue arrows.*

The u displacements between corresponding distorted dots was computed between each couple of consecutive frames and the x-axis strain rates were obtained adjusting Equation 2.3 to 1 dimension:

$$e_{xx} = \frac{\partial u}{\partial x} + 0.5 \left(\frac{\partial u}{\partial x} \right)^2 \tag{3.2}$$

Figure 15.b displays the heat maps of two frames of a 1N bump trial in the first columns and the corresponding average $\frac{d}{dt} e_{xx}$ patterns in the second column. Figure 15.c shows, in the first column, the displacement field curves applied to the dots for two different time steps of the simulation and the corresponding x-axis strain rates in the second column. The strain rates trends obtained from the simulation seem to match those found in the trials, therefore validating the hypothesis of loss of contact. These trials were thus discarded from the analysis, since the contact between the finger pad and the stimuli is a necessary condition for the success of the experiments and the correct interpretation of the results.

3.2 Sliding condition

Sliding condition trials were performed with a single plate speed of 5 mm/s and two Normal Forces of 1N and 5N. Trials with 1N of Normal Force produced $\frac{d}{dt}e_{xx}$ heat maps homogeneously close to zero across the finger pad area for both stimuli, up to the noise, except at the periphery of the elliptical ROI, were the contact with the plate was lost and the resulting strains were artifactual, due to optical distortion effects. The absence of strains suggests that 1N of Normal Force is not strong enough to cause any compression or stretch of the skin and therefore the finger pad slips over the bump and hole profiles smoothly. All trials with 5N of Normal Force, on the other end, manifested clear and consistent patters in correspondence of the stimuli, over a span of 23 frames ($\simeq 460$ ms) on average for the bump and of 16 frames ($\simeq 320$ ms) for the hole. Figure 16 panels a and b show typical x-axis strain rates heat maps over 6 frames for the bump and hole trials with 5N of Normal Force respectively, as well as the average trends corresponding to each frame. Similarly, frames from the remaining trials of both profiles are presented in Appendix B. The patterns appear to be symmetrical for the two designs: the bump generated a tendency to stretch in correspondence of its left side and to compression on its right side, while the hole caused an opposite trend of compression on its left side and of stretch on its right side. This is due to the symmetry of the profiles themselves: in fact, for both stimuli, compressive strains occur at their falling edge and tensile strains occur at their rising edge. Indeed, given the stimuli direction of motion from left to right, the falling edge of the profiles seems to act as an obstacle to the skin slippage, which therefore compresses, while the rising edge, on the other end, allows the skin to stretch, as illustrated in Figure 17.

Moreover, the 1D trends were further averaged across all frames associated with a pattern appearance of all the trails of the same stimulus, obtaining overall mean $\frac{d}{dt}e_{xx}$ trends for the bump and the hole, as displayed in Figure 16.c. Both curves show peaks of tensile and compressive x-axis strain rates of about 20 %/s.
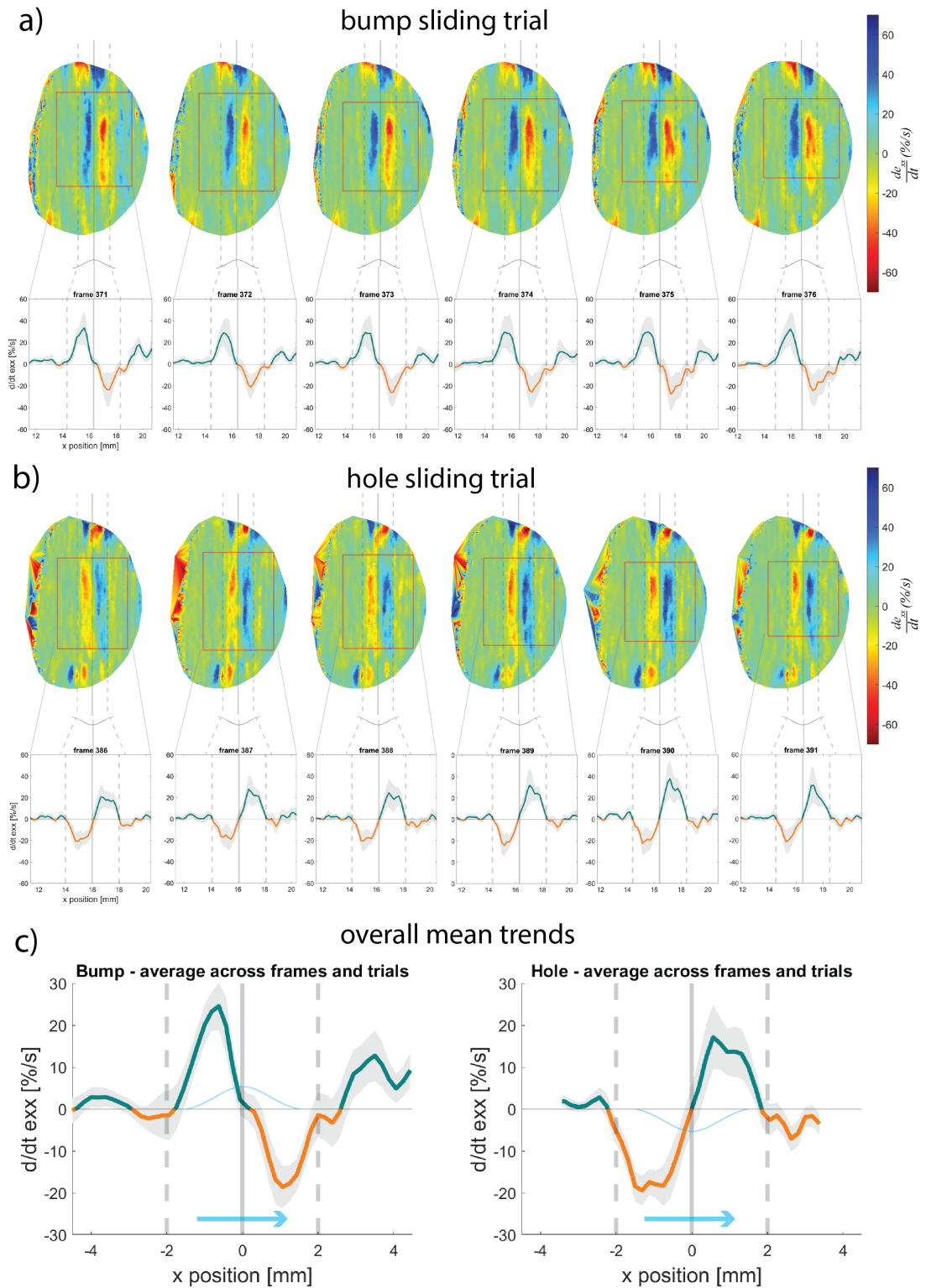
Figure 16: *Sliding condition patterns and overall mean trends. a) and b) Heat maps of 6 consecutive frames of a bump and a hole trial, respectively. The corresponding average patterns are displayed underneath each heat map.c) Overall mean trends for the bump (on the left) and the hole (on the right). For all panels, the gray solid vertical line corresponds to the center of the stimulus and the gray dotted vertical lines to its extremities, the bump and hole profiles are reported in light blue solid lines without a scale solely to indicate their position and their direction of movement is indicated with light blue arrows.*

38

Interestingly, the bump profile shows an additional tendency to stretch, circa 1mm to the right of the stimulus itself, though it is hard to assess whether this second peak (of around 10 %/s of amplitude) might be caused by the stimulus or not, considering also that it was observed solely in bump trials.
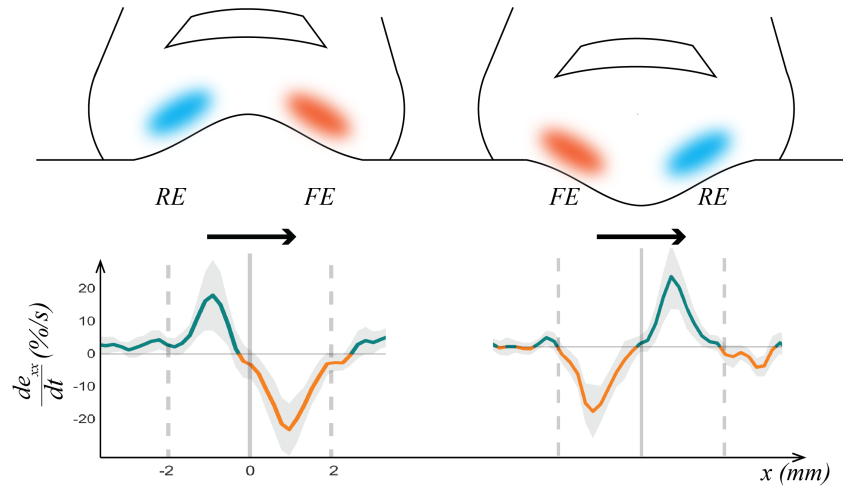
Figure 17: *Schematic of x-axis strain rates patterns. On the first row, RE and FE refer to the rising and falling edges of the stimuli profiles, black arrows indicate the direction of motion of the stimuli, red and blue ellipses correspond to portion of the skin under compression or stretch, respectively. On the second row, the associated typical x-axis strain rates trends.*

4 Discussion

This study investigated skin lateral deformations at high spatial and temporal resolution during tactile interaction with a bump and a hole profile. The experiment was restricted on a single subject and a limited amount of Normal Forces and plate speeds and serves as a *proof of concept* of the feasibility to apply strain rates computational algorithms, already established in the context of planar stimulation [2, 1, 3, 4], to stimuli of different geometries. It demonstrates that it's possible to manufacture specific stimuli profiles on flat plates ensuring the transparency of the part, crucial for the success of the procedure, in a cheap and reproducible manner, by means of 3D printing techniques and transparent resins. The use of non-planar geometries and a single camera set up implicated a series of complications, such as geometric and refractive distortions as well as distinct light reflections, which were successfully accounted for and corrected. The lateral skin strain rates could therefore be properly computed along the x-axis, and clear patterns of tensile and compressive strains were observed in Sliding condition trials with 5N of Normal Force, both in the bump and the hole, while no patterns emerged with 1N, suggesting a dependency of the strains occurrence to force intensity. The $\frac{d}{dt}e_{xx}$ patterns showed peaks of compression and stretch of roughly 20 %/s, which quantitatively fall into the ranges of strain rates already found in previous studies with planar stimulation under shearing [1, 3] and torsion [5]. Additionally, the patterns manifested a tendency of compression when the skin encounters a physical obstacle to its slippage over the plate, which, considering the direction of plate motion from left to right, corresponds to the falling edges of the two profiles, and a tendency of stretch in correspondence of the rising edges, where the changes in the geometry allow the skin to locally flow faster.

Furthermore, these results confirm what previously found by Léveseque *et al.* in their study [7]. They were able to capture high contrast images of the finger print while the finger was actively pressed and moved from left to right against transparent glass stimuli of similar shapes as those of this work. They extracted features from the finger pad images, tracked them between consecutive frames, and quantified the local skin deformations. For the bump profile, they observed a tendency of compressions when the skin interacted with the left side of the profile and a tendency of stretch when it interacted with the right side. They found the opposite trend for the hole design. Despite the lower spatial resolution, their findings are consistent with the present study: the compressive

40

and tensile deformations they measured occurred when the skin encountered the sides of the profiles that respectively hindered or facilitated the skin flow.

In Loaded condition trials, for all Normal Forces and plate speeds the presence of the bump and hole profiles interestingly did not cause any significant perturbation to the typical 'stick-to-slip' evolution already investigated with flat plates. This might be linked to the small dimensions of the profiles and further studies with bigger geometries might highlight strain patterns during the transition to full slippage as well. Additionally, finger pad skin in 1N Loaded condition trials with both plate speeds occasionally manifested partial loss of contact with the stimuli after reaching full slip, causing artifactual strains due to optical distortions that could be misinterpreted as actual lateral skin deformations. Thus, future work might utilize greater Normal Forces to ensure contact and avoid ambiguous results of difficult interpretation.

Microneurography recordings of the spiking activity of FA-I fast adapting afferents have demonstrated their correlation with lateral skin deformations in the corresponding receptive fields, with greater sensitivity to compression than stretch, and thus tangential strain rates are thought to provide useful information in the detection of slippage in the context of dexterous object manipulation and grip force modulation [3]. It can reasonably be assumed that the $\frac{d}{dt}e_{xx}$ patterns found in this study in 5N Sliding condition trials might generate as well a spiking response of FA-I afferents which therefore could be crucially involved in the recognition of surface geometry and texture during tactile exploration. The combination of the strain rate analysis performed in this study with microneurography would allow a precise assessment of the correlation between afferents spiking activity with the local lateral skin deformations with variagated stimuli geometries as well. Lastly, the absence of lateral deformations patterns during the 'stick-to-slip' transition suggests that the possible perception of the shapes could be also associated to skin deformations along the z-axis.

4.1   Perspectives and Limitations

The experimental procedure was performed using 1N of Normal Force with two plate speeds (5mm/s and 10 mm/s) and 5N of Normal Force with just one plate speed (5 mm/s). Concerning the Sliding condition, the 1N trials have proven to not produce significant strains patterns, and consequently a possible dependency of the patterns occurrence

and intensity to the stimuli speed after reaching full slip couldn't be investigated. Future works might extend the study of the phenomenon with multiple speeds and multiple Normal Forces, provided that they're greater than 1N. Moreover, this study was conducted on a single participant, but the procedure could be applied to multiple subjects to evaluate inter-subject variability, enabling further statistical analyses.

The manufacturing procedure (Section 2.1.2) introduced some defects on the surface of the transparent plate. In particular, not all the air inside the epoxy bath could be removed in the vacuum chamber: given the amount of epoxy-hardener mixture necessary to properly dip the plate inside the bath, the curing process made the mixture too viscous for gasses to escape the mix before all of the air was extracted. The remaining air inside the bath manifested as small air bubbles inside the epoxy coating after the dipping phase. Moreover, the curing process lasted several hours, during which small particles and dust could attach to the epoxy layer and remain stuck on the surface during its solidification, creating additional bubbles. As a consequence, small artifacts and distortions arose in the images in correspondence of these undesired bubbles, which could only partially be corrected by means of the calibration grid, therefore contributing to the noise in the data extracted from the images. A possible solution could consist in operating the air removal, dip coating and curing phase inside a clean room to avoid any interaction with external particles as well as employing different kinds of epoxy-hardener combinations with slower curing rates, allowing enough time for all the air to be removed from the bath inside the vacuum chamber. Additionally, a professional dip coating machine could be utilized to precisely tune multiple parameters during the dipping procedure such as the speed of the insertion of the plate in the bath, the amount of time the part is left still inside the mixture and the speed of the extraction phase, to obtain coating layers as uniform as possible and achieve better control on the thickness of the coat. Nevertheless, the dipping procedure performed 'by hand' produced satisfactory results.

Given the single camera set-up utilized in the experiments, the strains analysis computed on the images corresponds to the lateral skin deformations solely on the areas of contact between the finger pad and the plate. Specifically, where the plate is flat the position of the extracted features in the z-direction is constant, since the plate was mounted parallel to the image plane and set to a fixed height for all trials. Alternatively, in correspondence of the stimuli, where the plate is not flat, the effect of the 3rd dimension on the lateral

skin deformations analysis was accounted for thanks to the calibration process.

In the other regions of the fingertip, where the finger pad is not in contact, the information about the depth of the features isn't provided and can't be restored, preventing the possibility to reconstruct the deformations tangential to the skin. Moreover, where no contact with the plate is established, the changes in position of the features along the z-direction could result in apparent tangential skin movements due to optical distortions related to the refraction of light, ultimately leading to possible artificial strains computations if interpreted as part of the area actually in contact. Therefore, a key limitation of this study was the impossibility to precisely assess the contact area frame by frame, which resulted in the discard of strains data corresponding to regions of the images ambiguous between being in contact or out of contact. A possible way to address this issue could be the employment of two different scene illumination conditions that can switch at the same frequency as the camera's frame rate of acquisition [14]: one condition being a regular illumination from multiple directions, in combination with a speckles pattern applied to the finger pad, and the other one being a co-axial illumination, which theoretically allows high contrast images of the portions of the fingerprint in contact with the plate, as described in Section 2.3.3. Despite the limitations observed during preliminary test for this experimental set up to extract and track features, the images obtained from the co-axial configuration (Figure 11) could be used to outline the contact area, at least to a first approximation, with morphological operations and similar image processing techniques. By doing so, each trial acquisition would consist of the alternation of 'speckles' images, on which the same data analysis as the one of this study could be performed, and 'co-axial' images, which would provide the corresponding frame by frame evolution of the contact area, therefore allowing to restrict the strain analysis only to the regions of contact.

An alternative approach to quantify surface skin strains in the context of finger tip contact with 3-dimensional geometries could be the employment of a multi-view system [14]. Multiple cameras set in different positions and orientations would allow stereo vision, thus enabling to reconstruct the movements of the features along the 3D profiles, after proper calibration. Such set up would also facilitate to outline the contact area and no 'flattening' calibration process on the stimulus would be required, provided that the plate material and the coating material have similar refractive indices to avoid undesired light distortions at the interface between the two media that would hinder the stereo vision

3-D reconstruction. Moreover, light reflections would appear differently depending on the view and therefore should be corrected independently for each camera. In case of developable geometries like those subject of this study, light reflections would likely appear as straight bands of different orientations depending on the view. Thus, the attenuation process proposed in this work (see Section 2.3.2) could be adjusted to account for different light reflection orientations, e.g. employing kernels oriented accordingly to the direction of the reflections bands.

The light reflection attenuation processing performed on the images, therefore, substantially benefited from the geometry of the stimuli. Indeed, the reflections patterns observed on the trials manifested as long and consistent vertical lines, which allowed to isolate the information about the reflections intensity variations across the image by simply employing a vertical kernel to filter out the variations due to the speckles. This approach can't be applied to any generic stimulus shape, whose resulting reflections patterns depends on it specific geometry, and can't be easily extracted directly from the images themselves by low-pass filtering operations along a preferred direction. For example, tests on the dot shapes showed circular reflections patterns, which can't be extracted from the images by applying some sort of convolution. To account for this, during possible future experiments both with single and multi-view set-ups, each trail could be also performed without the participant's finger, that is, recording solely the moving plate against a plain dark background, to directly capture the frame by frame reflections patterns evolution of the stimulus. This *'ground truth'* recordings could then be used to compute a library of weight maps, uniquely associated with the stimulus positions throughout the trial (and possibly a specific view), to then properly attenuate the reflections of each frame in a similar fashion as that of this study, provided that the illumination of the scene remains constant. This approach would also avoid the issue of removing the effect of local light intensity changes due to the speckles.

5 Conclusions

Lateral skin deformations of the finger pad are believed to provide useful information about shapes and textures during tactile exploration. This study demonstrated the feasibility to manufacture transparent plates with small profiles embedded on their surface in an affordable manner, to acquire images of the finger pad during its interaction with the stimuli and to extract lateral skin strain rates, after successfully accounting for the technical challenges due to the presence of non-planar geometries. While the presence of the profiles didn't cause any significant deviation to the typical transition from a 'stuck' condition of the finger pad to full slippage, specific patterns of stretch and compression were observed due to the stimuli geometry after reaching full slip. In conclusion, this study therefore provides the tools and methodology to investigate lateral skin deformations during interaction with different shapes, detect and analyze the associated typical *compressive-tensile* patterns, and distinguish them from artifactual patterns of different origins.

A   Appendix - Alternative distortion correction methods

A.1   Mathematical reconstruction of the displacement fields with developable surfaces

Provided that the profile under study is a developable surface, its corresponding displacement field is constant along a given vertical axis and thus it can be simply modeled as a function of x (i.e. along the horizontal axis). This approach can be applied if the following conditions are met: (i) the geometry of the profile is known and the manufacture procedure can faithfully replicate it; (ii) the thickness of the coating layer can be precisely measured or estimated (for example, precisely measuring the profile before and after the dip coating procedure); (iii) the refractive indexes ratio between the plate material and the coating material is known or can be estimated precisely or, alternatively, the two materials appear to have refractive indexes similar enough that the light displacement component of the model can be neglected, reducing the distortion model to purely geometric displacement. The research of the right match between the two materials is thus crucial in this sense. These condition were not met in the present study, but the model is described and compared with the field obtained experimentally in the following paragraph for future works.

A simple model of the u-displacements between equally spaced dots along the profile and corresponding equally spaced dots on the horizontal axis was designed, referring to the Gaussian concave and convex shapes employed in the study, but the same derivations could be applied to any generic cross-sectional profile of a developable surface.

For both profiles, considering at first only geometric distortion (Figure 18.a, left panel), the displacement between a dot of the grid in position x_i on a flat surface parallel to the image plane and the projection of the same dot $\hat{x}_i$ when the gird is sitting on the Gaussian profile was computed as:

$$g(x_i) = \hat{x}_i - x_i \tag{A.1}$$

where $\hat{x}_i$ is the sum of the projections $\Delta\hat{x}_j$ of the distance between consecutive dots up to the $i - th$ position, considering the dots equally spaced of dx.

$$\hat{x}_i = \sum_{j=1}^{i} \Delta \hat{x}_j, \text{ with } \quad \Delta \hat{x}_j = p(\hat{x}_{j-1}) \cdot dx \qquad (A.2)$$
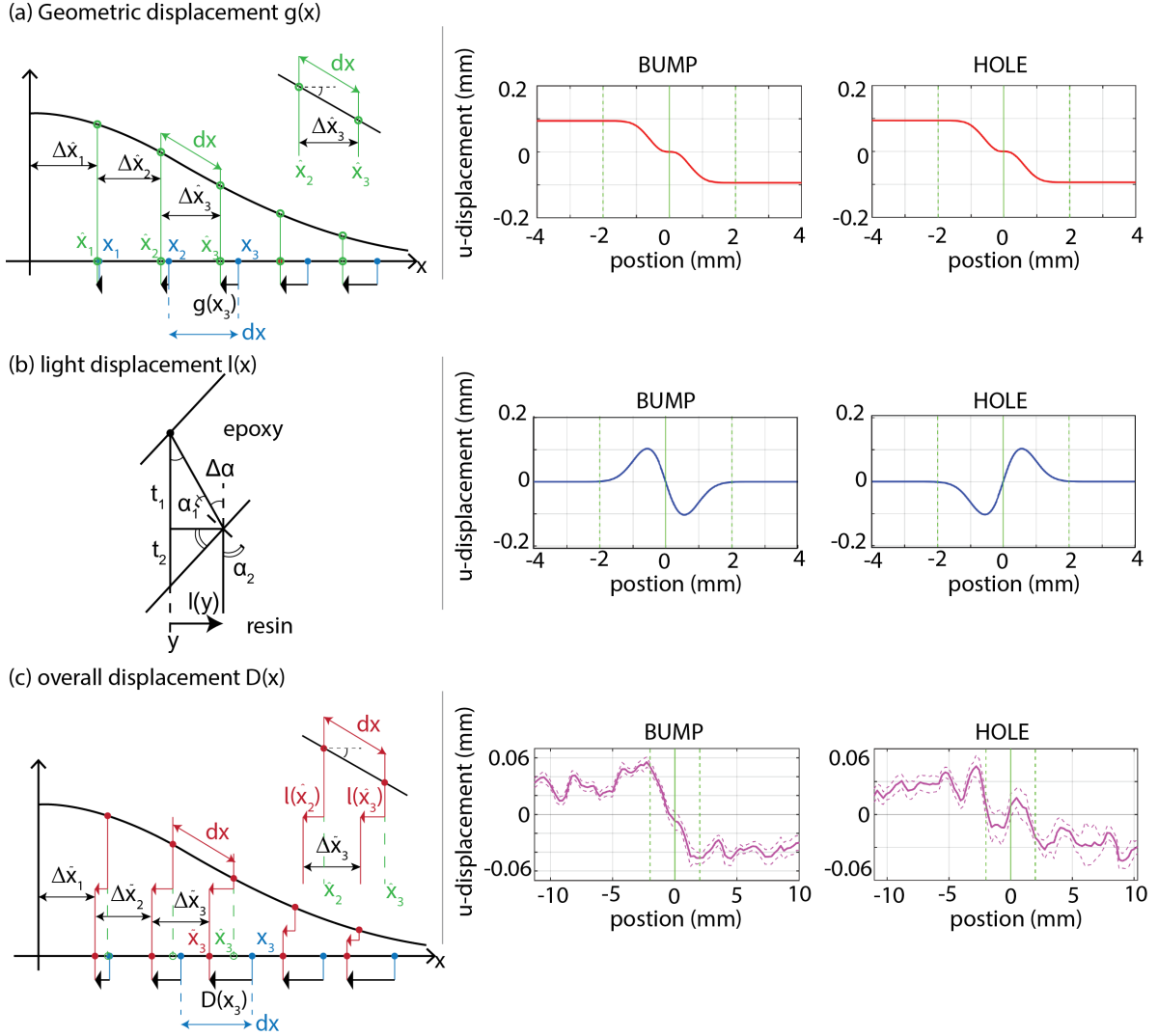
Figure 18: *Grid displacement model. (a) Geometric displacement. On the left, a schematic of the dots u-displacements due only to the geometry of the Gaussian profiles. On the right, the corresponding trends, computed numerically, of the u-displacements for the bump and the hole designs. (b) Light displacement. On the left, a schematic of the dots u-displacements due only to light refraction. On the right, the corresponding qualitative analytical trends for the bump and the hole. (c) Overall displacement. On the left, a schematic of the overall dots u-displacements as a combination of both geometric and light displacements. On the right, the empirical average calibration u-displacements for the bump and the hole, with the corresponding standard deviations in dotted lines. In all plots, the green solid line and the two green dotted lines represent, respectively, the center and the two extremities of the stimuli.*

The function $p(y)$ evaluates the proportion of the distance dx that is projected on the image plane as a function of the generic position y, which depends on the Gaussian

profile $G(y)$:
$$p(y) = cos\left(atan\left(\frac{d}{dy}G(y)\right)\right) = \frac{1}{\sqrt{1 + \left(\frac{d}{dy}G(y)\right)^2}} \tag{A.3}$$

The geometric displacement was then computed numerically and is shown in Figure 18.a (right panel) for both the bump and the hole Gaussian profiles.

Moreover, as introduced before, the difference in refraction indices between the plate resin and the thin layer of epoxy caused additional light distortion. A simple model of the displacement introduced by the light distortion in a generic position y on the rising edge of the Gaussian profile is proposed below.

By reference to Figure 18.b (left panel), y represents the position that a straight ray of light coming from a dot would reach on the image plane, if there was no change in material. Considering the deflection at the interface between the epoxy and the resin, the straight ray hitting the image plane is in position $y + l(y)$, with $l(y)$ being the light displacement of a dot in position y.

Given $\alpha_1(y)$ the angle of incidence travelling in the epoxy, $\alpha_2(y)$ the angle of refraction in the resin, and $\Delta\alpha(y) = \alpha_2(y) - \alpha_1(y)$ their difference, the thickness t of the epoxy layer is defined as:
$$t = t_1 + t_2 = l(y) \cdot tan(\alpha_2(y)) + \frac{l(y)}{tan(\Delta\alpha(y))} \tag{A.4}$$

Following Snell's Law of refraction (Equation A.5), with $\frac{\eta_2}{\eta_1}$ the ratio of the refractive indices of the two media, α_1 and α_2 are computed as in Equation A.6.

$$\frac{sin(\alpha_1)}{sin(\alpha_2)} = \frac{\eta_2}{\eta_1} \tag{A.5}$$

$$\alpha_1(y) = arcsin\left(\frac{\eta_2}{\eta_1} \cdot sin(\alpha_2(y))\right), \quad \alpha_2(y) = atan\left(\frac{d}{dy}G(y)\right) \tag{A.6}$$

The light displacement is then obtained from Equation A.4 as follows:

$$l(y) = \frac{t}{tan(\alpha_2(y)) + \frac{1}{tan(\Delta\alpha(y))}} \tag{A.7}$$

Assuming the refractive indices having similar values, the ratio $\frac{\eta_2}{\eta_1}$ is close to 1, thus $\Delta\alpha(y) \to 0$ and $\frac{1}{tan(\Delta\alpha(y))} >> tan(\alpha_2(y))$; the light displacement can therefore be simplified as:

$$l(y) \simeq t \cdot tan(\Delta\alpha(y)) \simeq t \cdot \Delta\alpha(y) \tag{A.8}$$

Given the symmetry of the Gaussian profile, similar derivations can be done for its falling edge as well, leading to a negative light displacement.

The light displacement curves were computed analytically from Equation A.7 for both the bump and the hole designs, as shown in Figure 18.b, right panel. It must be noted that neither the thickness t of the epoxy layer nor the ratio $\frac{\eta_2}{\eta_1}$ are known, and thus the two curves were computed setting arbitrarily the two parameters to 0.1 mm and 0.9 respectively, to investigate their qualitative trends and their effect on the overall displacement field. Specifically, the bump and the hole lead to opposite light displacement trends, given the opposite alternation of rising and falling edge of the Gaussian in the two profiles.

The overall displacement field, therefore, accounts for both the geometric and the light displacement (Figure 18.c, left panel):

$$D(x_i) = g(x_i) + l(\hat{x}_i) = \hat{x}_i - x_i + l(\hat{x}_i) \tag{A.9}$$

which can be re-arranged, by analogy with Equation A.1, as:

$$D(x_i) = \tilde{x}_i - x_i = \sum_{j=1}^{i} \Delta\tilde{x}_j - x_i \tag{A.10}$$

with

$$\Delta\tilde{x}_j = \Delta\hat{x}_j + l(\hat{x}_j) - l(\hat{x}_{j-1}) = \left[p(\hat{x}_{j-1}) + \frac{l(\hat{x}_j) - l(\hat{x}_{j-1})}{dx} \right] \cdot dx \tag{A.11}$$

The u-component of the displacement filed obtained from the calibration grid is thus expected to be a combination of the geometric and light distortion trends for both profiles, as in Equation A.9. The right panel of Figure 18.c displays again the average calibration u-displacements of the bump and the hole, which appear to be qualitatively the combination of the expected curves showed in the panels above, even though the amplitudes of the modeled and experimental trends don't correspond. This might be due to two main reasons. First, the actual height/depth as well as the width of the bump and the hole were not precisely measured and variation from their nominal size would cause a change in the amplitude of the geometric displacements; more specifically, smaller profiles lead to smaller amplitudes at the two tails of the geometric and overall trends, with respect to what predicted in the models (~ 0.09 mm). Moreover, the layer of epoxy makes the bump profile slightly higher and the hole profile slightly less deep, explaining the difference in amplitude of the tails of the experimental overall u-displacements between the two

designs (~ 0.04 mm and ~ 0.02 mm respectively). Second, as explained above, the light refraction displacement is not know in amplitude, thus the corresponding expected curves are intended to be interpreted apart from a multiplicative factor, as well as their contribution to the overall displacements.

The calibration displacement field is directly linked with the undesired displacements of the features due to geometry and light refraction observed during the trials.

Considering a completely flat surface, between two consecutive frames of a trial the plate moves of a distance dx in the ulnar-radial direction under the finger, and, if the fingertip is perfectly sliding over the surface, no contraction or distention of the skin occurs. Therefore, with respect to the moving surface, the speckles are travelling the same distance dx in the opposite direction. Thus, no displacement of the speckles is tracked between the two frames and consequently the strains of the features are computed to be zero (features tracking and strains computation are covered in details in Section 2.3.3). When a feature slides of dx over the bump or the hole, instead, because of the geometry of the profiles and the effect of light refraction, a non-zero artificial u-displacement $u(\tilde{x}_i)$ of the feature is tracked between two consecutive frames (Figure 19), which can be computed as in Equation A.12, leading to 'apparent' and untrue strains computation.

$$u(\tilde{x}_i) = dx - \Delta\tilde{x}_i = dx - \left[p(\hat{x}_{i-1}) + \frac{l(\hat{x}_i) - l(\hat{x}_{i-1})}{dx} \right] \cdot dx \qquad (A.12)$$
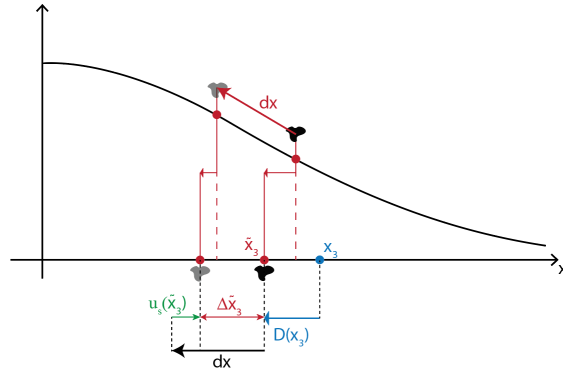
Figure 19: *Artificial feature displacements model. Schematic of the finger sliding of dx over the Gaussian profile (in reality the finger is still and the plate moves of dx). Black and gray speckles represent the initial and final positions, spaced by dx, of a general feature starting from $\tilde{x}_3$ when moving along the Gaussian profile, as well as its initial and final positions on the image plane due to the optical deformations, spaced of $\Delta\tilde{x}_3$. The difference in length between dx and $\Delta\tilde{x}_3$ generates an artificial displacement of the feature.*

Indeed, specific artifacts in the features tracking can be expected and, even though

they can't be directly obtained from Equation A.12 since the function $l(y)$ is not known, they can be derived from the calibration u-displacement fields.

With reference to Figure 18.c (left panel), $D(x_i)$ can be re-written, from Equations A.10 and A.11, as:

$$
\begin{aligned}
D(x_i) &= \sum_{j=1}^{i} \left[p(\hat{x}_{j-1}) + \frac{l(\hat{x}_j) - l(\hat{x}_{j-1})}{dx} \right] \cdot dx - x_i \\
&= \sum_{j=1}^{i} \left[p(\hat{x}_{j-1}) + \frac{l(\hat{x}_j) - l(\hat{x}_{j-1})}{dx} - 1 \right] \cdot dx
\end{aligned}
\tag{A.13}
$$

with $x_i = \sum_{j=1}^{i} dx$. We can then define the derivative of the u-displacement field as:

$$
\frac{d}{dx} D(x_i) = p(\hat{x}_{i-1}) + \frac{l(\hat{x}_i) - l(\hat{x}_{i-1})}{dx} - 1
\tag{A.14}
$$

and, from Equations A.12 and A.14:

$$
u(\tilde{x}_i) = dx \cdot \left[-\frac{d}{dx} D(x_i) \right], \quad \text{with} \quad \tilde{x}_i = x_i + D(x_i)
\tag{A.15}
$$

The average calibration u-displacement fields of the bump and the hole were smoothed to reduce their noise and their derivative was computed. The supports of the derivatives in the variable x_i were then 're-mapped' to the corresponding $\tilde{x}_i$ and thus the expected feature displacement artifact could be obtained from Equation A.15, with dx equal to the distance travelled by the plate between consecutive frames.

Figure 20 a and b display the calibration u-displacement fields as well as the expected features displacement artifacts for the two designs, to be compared with the average u-displacement artifacts found with feature tracking during bump and hole trials computed on the raw images: for both designs, a region of interest was selected after feature tracking and the u-displacements of the features falling into the ROI were computed as the distance they travelled in the x direction after 3 frames, corresponding to a plate movement of $dx \simeq 0.1$ mm. The u-displacement fields obtained (Figure 20 e and f) were then averaged along the y-axis (Figure 20 c and d). Indeed, the expected trends of the artifacts match those found in the trials.
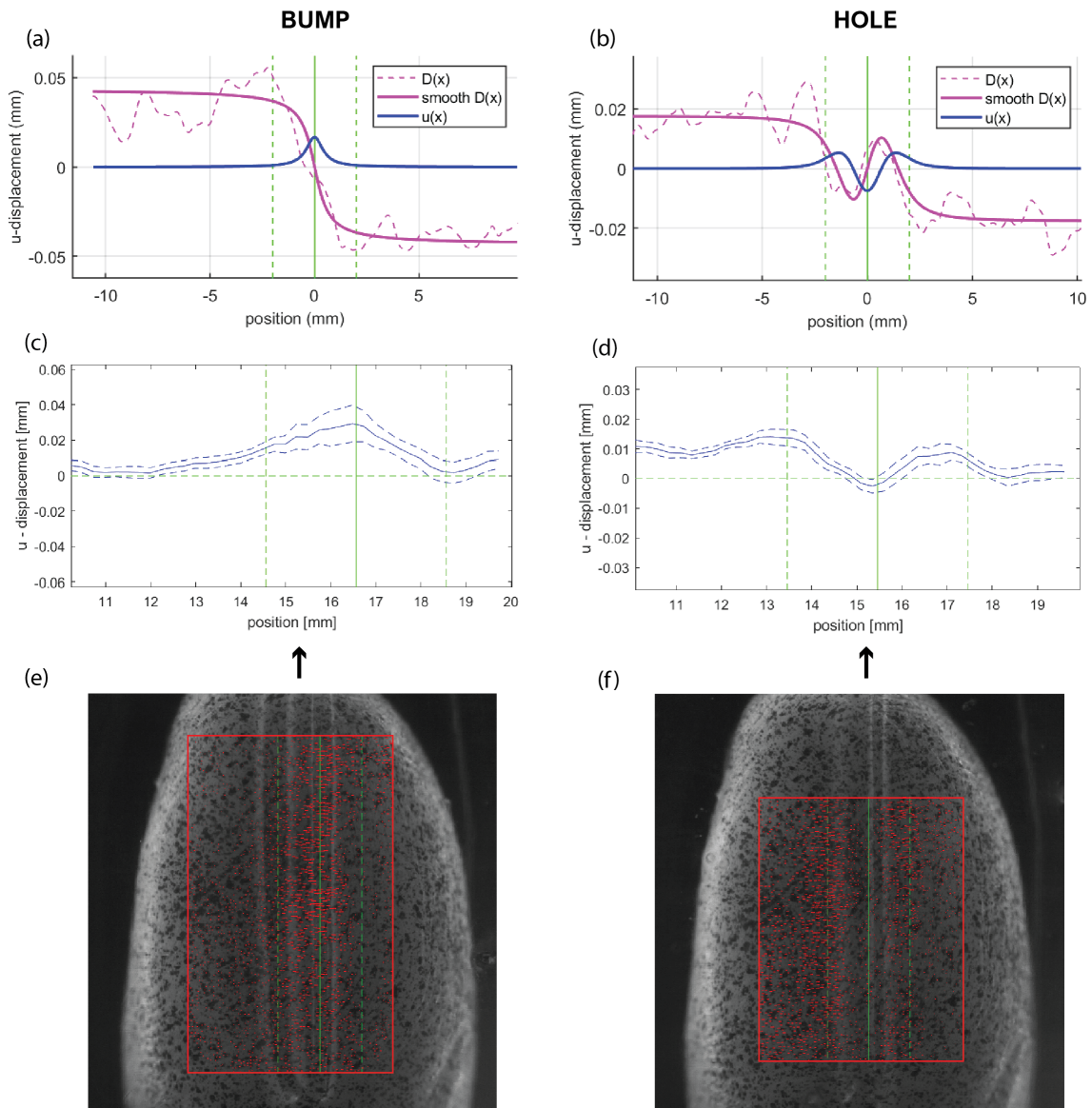
Figure 20: *Artificial feature displacements in trials. (a) and (b) display, for the bump and the hole respectively, the average calibration u-displacements (dotted magenta line), the corresponding smoothed trend (solid magenta line) and the expected artificial features u-displacements (solid blue line). (c) and (d) show, for the bump and the hole respectively, the average artificial features u-displacements patterns (solid line) found in the trials. The dotted lines represent the standard deviations. (e) and (f) display one frame from the bump and the hole trials respectively, with superimposed the ROI (red box) in which features were selected to compute their u-displacements in a span of 3 frames. Red arrows correspond to the u-displacements of each feature. The resulting u-displacement field was averaged along the y-axis of the ROI to obtain the trends in (c) and (d). In all panels, the green solid line and the two green dotted lines represent, respectively, the center and the two extremities of the stimuli.*

52

A.2 Distortion correction with non-developable surfaces

For a generic non-developable 3D profile, a flat grid cannot be applied without warping, meaning the surface cannot be flattened while preserving internal distances and areas. As a result, a displacement field cannot be determined experimentally or mathematically. Therefore, in this paragraph an alternative approach is proposed, which requires that the following conditions are met: (i) the geometry of the profile is known and the manufacturing procedure can faithfully replicate it; (ii) the thickness of the coating layer can be precisely measured or estimated; (iii) most importantly, the two materials appear to have refractive indexes similar enough that the distortions due to light refraction can be neglected. In such way, the geometry of the stimulus is fully defined by the analytical definition of its profile plus the thickness of the coating. Therefore, the position of the features on the image plane can be back projected onto the overall 3D surface (including the additional coating thickness), obtaining their (x,y,z) positions and therefore reconstructing the actual relative distances and areas to properly compute the skin deformations (Figure 21).
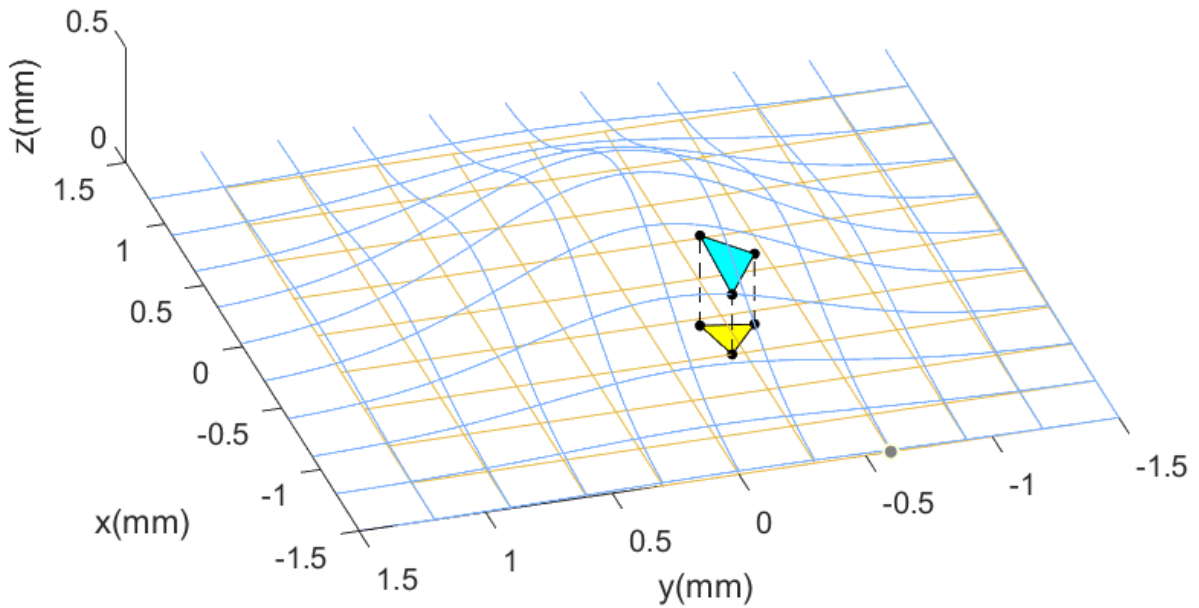
Figure 21: *Features back projection. As an example, the dot geometry manufactured on the plate, $z(x,y) = 0.5mm \cdot e^{-\frac{x^2+y^2}{(0.8mm)^2}}$, is represented with a blue grid and the image plane is represented with a ocher grid. The area between three generic features on the image plane is shown in yellow. The cyan area represent the actual area between the features after back projecting them on the 3D stimulus profile.*

Next, the strain rates computation is obtained extending Equations 2.2 and 2.3 to 3D

space:

$$G_u = \left(\frac{\partial u}{\partial x}, \frac{\partial u}{\partial y}, \frac{\partial u}{\partial z} \right), \quad G_v = \left(\frac{\partial v}{\partial x}, \frac{\partial v}{\partial y}, \frac{\partial v}{\partial z} \right), \quad G_w = \left(\frac{\partial w}{\partial x}, \frac{\partial w}{\partial y}, \frac{\partial w}{\partial z} \right) \tag{A.16}$$

$$e_{xx} = \frac{\partial u}{\partial x} + 0.5 \left[\left(\frac{\partial u}{\partial x} \right)^2 + \left(\frac{\partial v}{\partial x} \right)^2 + \left(\frac{\partial w}{\partial x} \right)^2 \right] \tag{A.17}$$

where u, v and w are the displacements along the x, y and z axes, respectively.
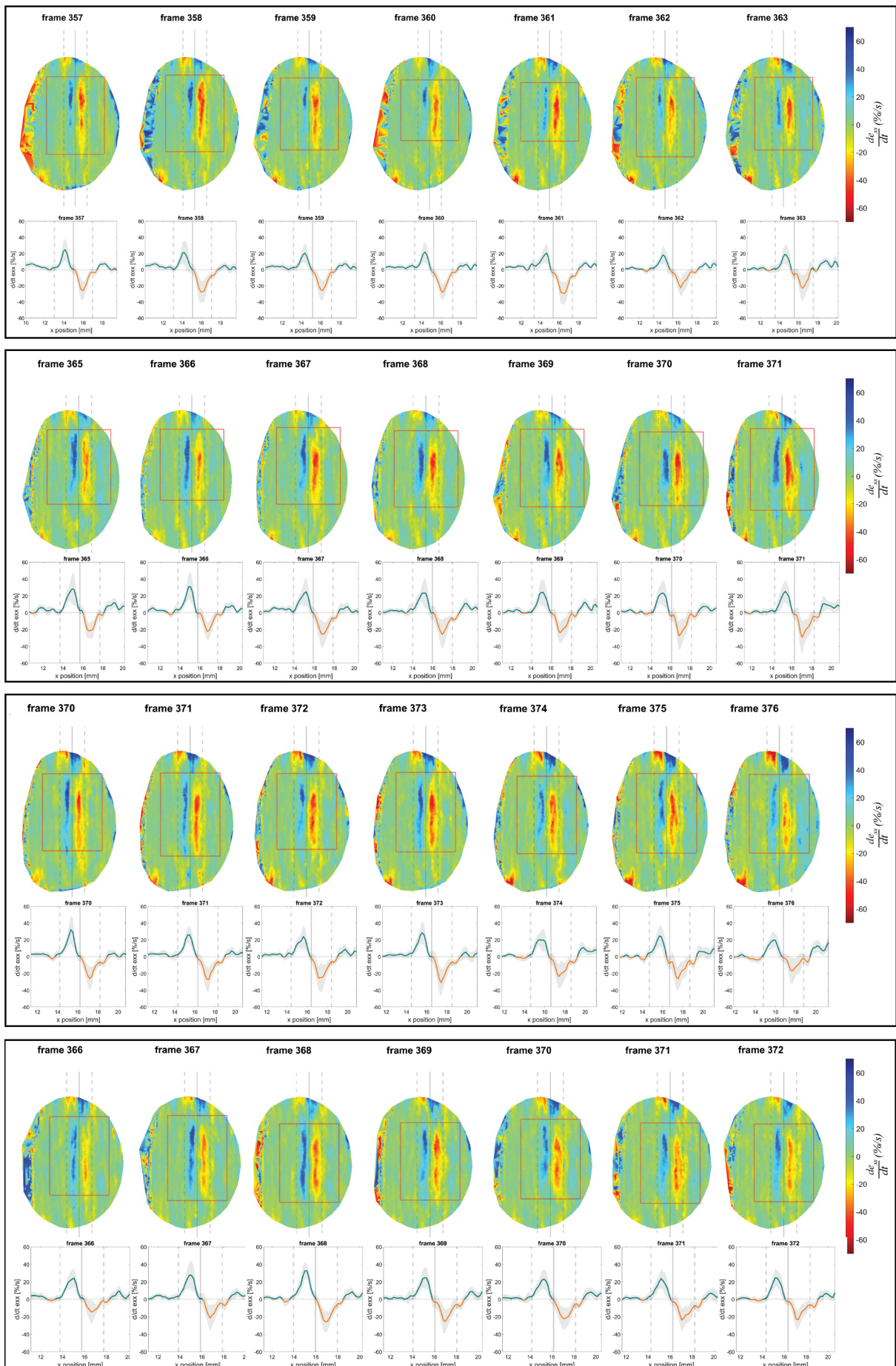
B   Appendix - Results, sliding condition trials

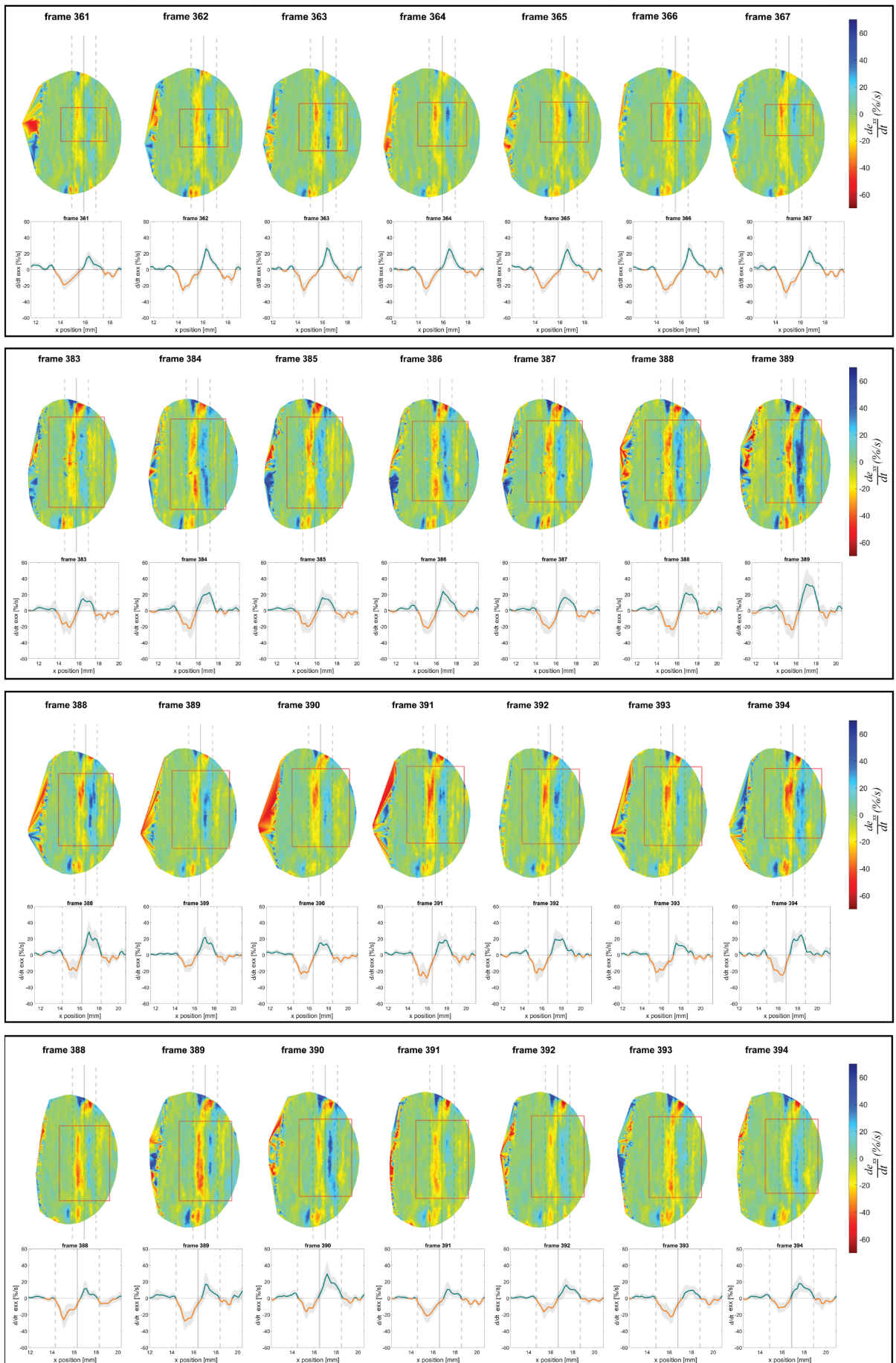**Figure 22:** *Bump - Sliding condition trials*

Figure 23: *Hole - Sliding condition trials*

References

[1] Benoit Delhaye, Allan Barrea, Benoni B Edin, Philippe Lefevre, and Jean-Louis Thonnard. Surface strain measurements of fingertip skin under shearing. *Journal of The Royal Society Interface*, 13(115):20150874, 2016.

[2] Benoit Delhaye, Philippe Lefevre, and Jean-Louis Thonnard. Dynamics of fingertip contact during the onset of tangential slip. *Journal of The Royal Society Interface*, 11(100):20140698, 2014.

[3] Benoit P Delhaye, Ewa Jarocka, Allan Barrea, Jean-Louis Thonnard, Benoni Edin, and Philippe Lefèvre. High-resolution imaging of skin deformation shows that afferents from human fingertips signal slip onset. *Elife*, 10:e64679, 2021.

[4] Allan Barrea, Benoit P Delhaye, Philippe Lefèvre, and Jean-Louis Thonnard. Perception of partial slips under tangential loading of the fingertip. *Scientific reports*, 8(1):7032, 2018.

[5] Sophie du Bois de Dunilac, David Córdova Bulens, Philippe Lefèvre, Stephen J Redmond, and Benoit P Delhaye. Biomechanics of the finger pad in response to torsion. *Journal of the Royal Society Interface*, 20(201):20220809, 2023.

[6] Giulia Corniani, Zing S Lee, Matt J Carré, Roger Lewis, Benoit P Delhaye, and Hannes P Saal. Sub-surface deformation of individual fingerprint ridges during tactile interactions. *bioRxiv*, pages 2023–07, 2023.

[7] Vincent Levesque and Vincent Hayward. Experimental evidence of lateral skin strain during tactile exploration. In *Proceedings of EUROHAPTICS*, volume 2003, pages 6–9. IEEE Dublin, 2003.

[8] Steven C Hauser and Gregory J Gerling. Imaging the 3-d deformation of the finger pad when interacting with compliant materials. In *2018 IEEE Haptics Symposium (HAPTICS)*, pages 7–13. IEEE, 2018.

[9] Nikolas M. Patrikalakis, Takashi Maekawa, and Weizhong Cho. *Shape Interrogation for Computer-Aided Design and Manufacturing*. Springer, 2002. Accessed: 2025-02-28.

[10] M Tada and T Kanade. An imaging system of incipient slip for modelling how human perceives slip of a fingertip. In *The 26th annual international conference of the IEEE engineering in medicine and biology society*, volume 1, pages 2045–2048. IEEE, 2004.

[11] Jianbo Shi and Tomasi. Good features to track. In *1994 Proceedings of IEEE conference on computer vision and pattern recognition*, pages 593–600. IEEE, 1994.

[12] Jean-Yves Bouguet et al. Pyramidal implementation of the affine lucas kanade feature tracker description of the algorithm. *Intel corporation*, 5(1-10):4, 2001.

[13] Gary Bradski and Adrian Kaehler. *Learning OpenCV: Computer vision with the OpenCV library.* " O'Reilly Media, Inc.", 2008.

[14] Donatien Doumont, Anika R Kao, Julien Lambert, Francois Wielant, Gregory J Gerling, Benoit P Delhaye, and Philippe Lefevre. 3-d reconstruction of fingertip deformation during contact initiation. *bioRxiv*, pages 2025–02, 2025.